Article:

The evolution and characterisation of the corrosion scales formed on 3Cr steel in CO$_2$-containing conditions relevant to geothermal energy production

Yong Hua[a]*, Xiaoqi Yue[c], Huifeng Liu[a, b], Yang Zhao[d], ZeZhou Wen[a], Yongxing Wang[a], Tao Zhang[d]*, Lei Zhang[c]*, Jianbo Sun[b]* and Anne Neville[a]

a: Institute of Functional Surfaces, School of Mechanical Engineering, University of Leeds, Leeds, LS2 9JT, United Kingdom.
b: School of Materials Science and Engineering, China University of Petroleum (East China), Qingdao, China.
c: Institute of Advanced Materials and Technology, University of Science and Technology Beijing, Beijing, 100083, China.
d: Shenyang National Laboratory for Materials Science, Northeastern University, 3-11 Wenhua Road, Shenyang 110819, China.

*Corresponding author: Yong Hua: Y.Hua@leeds.ac.uk;
Tao Zhang: zhangtao@mail.neu.edu.cn;
JianboSun: sunjianbo@upc.edu.cn.
Zhang Lei: zhanglei@ustb.edu.cn;

Abstract

The corrosion behaviour of 3Cr steel at CO$_2$ partial pressures (p_{CO2}) of 2.7/28.5 bar and 200°C was investigated. The evolution of double-layered corrosion scales was analysed by surface analysis to identify physical and chemical nature and results are combined with an analysis of thermodynamic calculations. Both experimental and thermodynamic results show that the corrosion scales comprise a crystalline FeCO$_3$ outer layer and an inner Fe$_3$O$_4$, FeCr$_2$O$_4$, and Cr(OH)$_3$ at 2.7 bar p_{CO2}. At 28.5 bar p_{CO2}, the inner layer evolves to be a mixture of FeCr$_2$O$_4$ and Cr(OH)$_3$ containing concentrated Cl$^-$ ions, and this induces an enhancement of localised corrosion.

Keywords: 3Cr steel, CO$_2$ corrosion, corrosion scales, inner layer evolution

1.0 Introduction

The corrosion behaviour of pipeline and tubing steels in CO_2-containing geothermal environments has received significant attention, yet the control of material corrosion remains an important issue for researchers due to the essentially complicated corrosion processes.[1] Considering economic savings, to find a low-cost material with improved corrosion resistance is one of the logical and key strategies for corrosion control to geothermal energy production.

Several researchers reported the variation of chromium (Cr) content on influence of corrosion resistance for different low alloy tubing. [1-10] To date, researchers have considered to replace carbon steel by 1-5% Cr steels based on their improved corrosion resistance and enlarge the scope of applications. This is important as demands for corrosion resistance material from renewable energy sources such as geothermal. Materials must provide the required performance while proving to be an economic alternative. Recently, 3Cr steel has become one of the common potential candidates because it is significantly cheaper than stainless steel and has promising improved corrosion protection compared to carbon steel within oil and gas application.

Several works have been conducted to evaluate the corrosion behaviour in terms of general and localised corrosion of 3Cr steels under high temperature and high pressure (HTHP) environments and to understand the corrosion mechanisms or the corrosion product formation in CO_2-saturated aqueous environments.

1.1 Research reviews relevant to general corrosion behaviour of 3Cr steels in CO_2 environments

Xu et al.[1] investigated the corrosion behaviour of two 3Cr steels (Bainite-Ferrite (BF) and Ferrite-Pearlite (FP) microstructures) in CO_2-saturated conditions at 80 °C and 8 bar. They found that the

2

formation of the corrosion product scales reduces corrosion rates and suggested that the observed

low corrosion rates are attributed to enrichment of Cr within the corrosion scales which this layer

can protect to the steel. Their report recommended that BF-3Cr steels provide better corrosion

resistance than FP-3Cr steels. Muraki et al.[2] indicated that an increase in Cr level from 0 to 5%

progressively decreases the general corrosion rates, and mainly due to forming protective corrosion

product scales and suggested that this enriched Cr layer effectively suppresses the general corrosion

rate. Takabe and Ueda[3] compared the general corrosion rates of low Cr-bearing steels in the CO_2

environment a 60 °C and 100 °C with test periods of 24, 48, 96 and 720 hours. Results showed that

the general corrosion rate was reduced by increasing the Cr content and the enriched Cr was

observed in the protective corrosion product scales. Kermani et al.[4] reported the corrosion

behaviour of 3Cr steel for 1 and 22 months in actual field conditions and the results indicated that

the protective Cr rich layer on the steel surface is stable and capable of forming at a relatively low

pH such as 3.8. One important message from Kermani et al's[4] work for 3% Cr steel was related to

the economics of the alloy, 3Cr steel has less than 1.5 times cost penalty compared to conventional

grades of carbon steel, with promising improved corrosion protection by 3 to 40 times compared to

carbon steel in oil & gas applications. Zhu et al.[5] tracked the film growth at 80 °C and 8 bar of p_{CO2}

via the EIS method and divided the formation processes of the film into three periods; dynamic

adsorption, an incomplete-coverage film and a fully covered film. Their results suggested that the

fast dissolution process of 3Cr steels mainly occurs in the first 2 hours with the absence of film or

the surface was covered by an incomplete-coverage film. Guo et al's work[6] in the same condition

further clarified that corrosion product scales include an inner $Cr(OH)_3$ layer (containing nano-

quasicrystalline and nanocrystalline grains) and outer $FeCO_3$ crystals precipitated on the inner layer,

3

72 suggesting that the decrease in anodic dissolution current over long periods was due to the inner

73 layer than the outer $FeCO_3$ layer. Lu et al.,[7] used electrochemical measurements to examine 3Cr

74 steels under 3 bar CO_2 at various temperatures up to 90 °C. Their corrosion rates increased with

75 rising the temperatures. A double-structure corrosion product layer was observed at low

76 temperatures of 30-50 °C, it can be noted that a single $FeCO_3$ layer was reported at 70-90 °C.

77 Liu et al.[8] conducted long-term corrosion tests from 168 hours to 1008 hours at 80°C, 2.3 bar CO_2

78 partial pressure, and a velocity of 2.5 m/s and the results suggested that a three-layered structure

79 can be observed. Both inner and outer layers are identified as $FeCO_3$, and the enrichment of Cr is

80 exhibited in a cement-like middle layer and mixture with $FeCO_3$. Li et al.,[9] performed corrosion tests

81 on 3Cr exposed to CO_2-saturated solutions at 8 bar CO_2 and 80 °C for 240 hours. They reported that

82 3Cr with a martensite microstructure has the best corrosion resistance compared to other types of

83 3Cr with bainite or ferrite/pearlite microstructure. Wang et al.,[10] indicated that the addition of Ca^{2+}

84 can change the morphology and composition of the corrosion products on the surface. The initial

85 corrosion rates were measured smaller due to the presence of Ca^{2+} compared to that of the absence

86 of Ca^{2+} condition, suggesting the Ca^{2+} ions accelerate the precipitation of initial corrosion scales. As

87 for the harsh conditions for low Cr bearing alloys, Hua et al.[11] reported the poor corrosion

88 resistance of low Cr steels, including 3Cr, at 60°C and 100 bar CO_2 and indicated that the low Cr

89 steels cannot provide better corrosion resistance compared to X65 carbon steel over long term

90 exposure.

91 **1.2 *Research review on the localised corrosion behavior of 3Cr steels in CO₂ environments***

4

In 2001, Takabe and Ueda[3] studied the corrosion product formation for C-Mn steel and 1-5% Cr steels with martensitic microstructure at 60 °C and 100 °C and various immersion times. The results indicated that the Cr content within the inner corrosion product scale increases from 12.5% to 50 % mass Cr. 3Cr and 5Cr steels provide better localised corrosion resistance than 1Cr steel. The work of Chen et al.[12] showed that Cr content in the steel increased up to 4% results in improved pitting resistance. The formation of protective corrosion scales is comprised of $Cr(OH)_3$, Cr_7C_3, $FeCO_3$ and Cr_2O_3 and the inner layer is mainly $Cr(OH)_3$. The results suggested that the inner layer was responsible for significantly improving the pitting resistance. Lin et al.,[13] conducted experiments for 3Cr exposed to the solution containing CO_2-O_2. They reported that the presence of O_2 reduces the corrosion product protection to the steel surface. The dissolved 5% O_2 increases the pitting corrosion occurring on the surface due to the measured nonuniform Cr-rich areas. Wei et al.,[14] performed the experiments for X70, 3Cr and 6.5Cr steels exposed to CO_2-saturated solution at 80 °C and pressure of 100 bar. The results indicated that the additional 3Cr increases the general corrosion rate, but the localised corrosion decreases under the flow rate of 1 m/s. The corrosion rates were decreased significantly as Cr content increased to 6.5 wt.%. An inner Cr-rich layer was proved to protect the localised corrosion. The results from Hua et al.[11] in a 100 bar CO_2 condition suggested that the Cr-riched inner layer formed on 3Cr and 5Cr steels appears to accelerate the pit propagation. The formation of the inner layer with increasing Cr content is less dense and compact compared with $FeCO_3$ formed on carbon steel thus failed to improve localised corrosion resistance at 60°C and CO_2 partial of 100 bar. Similarly, the results of Liu et al.[8] revealed the $Cr(OH)_3$ locally co-precipitated with $FeCO_3$ over long exposure times and the presence of co-precipitated corrosion scales increases the localised corrosion.

114 Based on the literature above, 3Cr steel is considered as an improved corrosion resistance

115 alternative to carbon steel, whilst it is significantly cheaper than stainless steels. However, little

116 information exists in the literature relating to the corrosion behaviour in terms of general and

117 localised corrosion for 3Cr steels exposed to conditions that reflect geothermal environments

118 (where temperatures > 150 °C). The purpose of this research is to fill this knowledge gap via studying

119 the protective capability of the corrosion product scales formed on 3Cr steel surfaces at various CO_2

120 partial pressures as well as the corrosion capabilities of 3Cr steel in terms of the general and

121 localised corrosion behaviour under a high temperature (200°C) CO_2 environment. We have also

122 merged the results from the detailed characterisation of the physical and chemical nature of the

123 corrosion scales with an analysis of Pourbaix diagrams. We propose a CO_2 corrosion mechanism for

124 3Cr steels immersed in CO_2-saturated solution, clarifying that the Cl^- ions induce localised corrosion

125 at HTHP.

126 ## 2.0 Experimental procedure

127 ### 2.1 material and methods

128 The elemental compositions of 3Cr steel are 0.21 wt.% Si, 0.24 wt.% C, 0.005 wt.% P, 0.0015 wt.% S,

129 0.53 wt.% Mn, 3.1 wt.% Cr and balance with Fe, its microstructure as shown in Figure 1. The disc

130 sample with a 25 mm diameter and 5 mm in thickness.

131 The sample surface was wet-ground to 1200 grit SiC abrasive paper. It was then abraded with a 3μm

132 diamond suspension to achieve a mirror finish. According to the ASTM E3-01[15] and E407-99

133 standards[16], the etchant solution was 3% Nital and the sample was immersed in the Nital solution

6

134   for 15s. The microstructure image of 3Cr steel was performed via a LEICA DM 6000M upright optical

135   microscope. Carbides are randomly distributed within the 3Cr steel as shown in Figure 1.
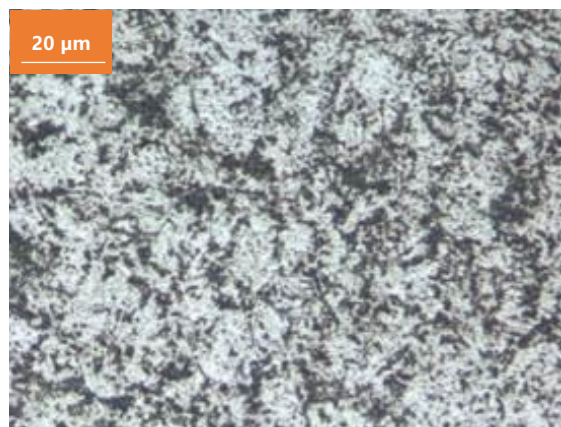
136

137   **Figure 1. The microstructure of 3Cr steel.**

138   Figure 2 represents the whole autoclave setup. The experimental procedure can be found in our

139   previous publications[17, 18]. The ratio of the volume of the solution to the sample area was 33mL/cm^2.

140   The experimental matrix is provided in Table 1. The predicted pH and Pourbaix diagrams were

141   calculated by using OLI software.[24] The considered species to generate the diagrams have been

142   provided in Table S1 in the supplementary document.
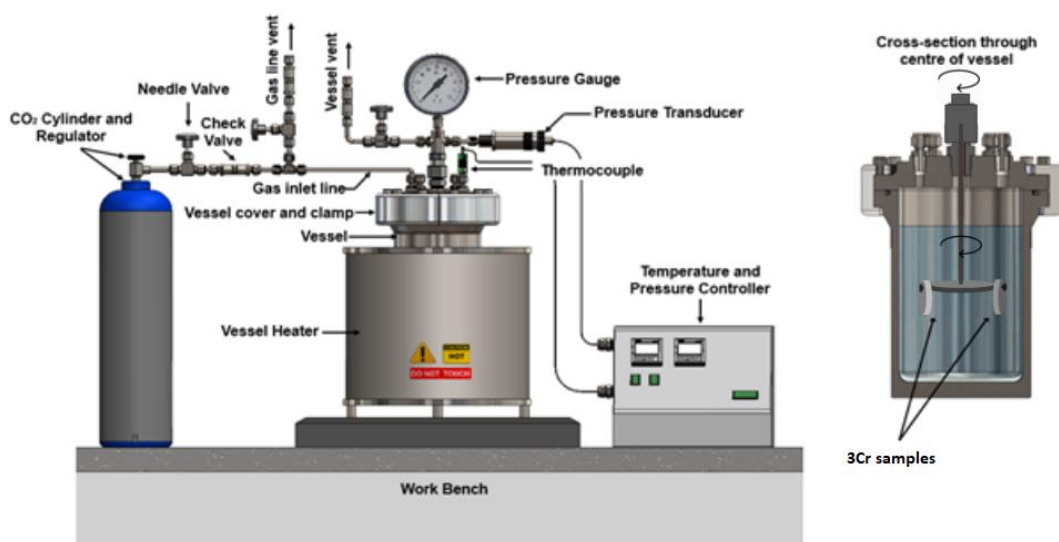
143

144   **Figure 2. A schematic diagram of the experimental setup for the corrosion tests.** [17, 18]

Table 1: Test conditions

Brine (mg/L)	Temp, °C	CO$_2$ pressure at 25 °C, bar	pH	CO$_2$ pressure at 200°C, bar	Total pressure at 200°C, bar	Immersion time, hours
NaCl solution: Cl-: 29503, NaHCO3:585	200	1	6.41	2.7	18	5/20/48/120
		20	5.39	28.5	46	

After immersion tests, the autoclave was cooled down to 80 °C within 10 minutes, followed by the depressurisation of the vessel. The corroded specimens were immediately rinsed with distilled water and dried with compressed air. The corrosion scales were removed according to ASTM G1-03 standards[19] using Clark's solution (20 g antimony trioxide + 50 g tin(II) chloride + 1000 ml 38% hydrochloric acid). The corrosion rate was calculated by the following equation.

$$R_{\mathrm{corr}} = \frac{8.76 \times 10^7 \times \Delta m}{S \times T \times \rho} \tag{1}$$

Where R_{corr} is the general corrosion rate, mm/year; Δm is the weight loss, g; S is the exposed surface area, cm^2; ρ is the density of the steel, g/cm^3; and T is the immersion time, hours.

2.2 Surface analysis

One sample with covered corrosion scales from each condition was used to perform surface analysis. The characterisation of morphology and chemical composition via a combination of scanning electron microscopy (SEM), energy-dispersive X-ray spectroscopy (EDX) throughout a Carl Zeiss EVO MA15 SEM combined with a focused ion beam (FIB) would contribute an important part of this study. In addition, the composition and state of naturally formed corrosion scales were analysed by X-ray diffraction (XRD) and Raman spectroscopy respectively.

161 After the removal of corrosion scales, profilometry measurements were conducted by an NPFLEX

162 3D Surface Metrology System. According to ASTM Standard G46-94 [20], the top 10 deepest pits were

163 used for the pitting depth characterisation of scanned areas from each sample. The localised

164 corrosion rates were calculated by using Equ (2)

$$Rr_L = \frac{8.76 \times D}{T} \tag{2}$$

165 Where Rr_L is the localised corrosion rate, mm/year; D is the average localised/pitting depth of ten

166 deepest pits from the sample in μm; T is immersion time in hours.

3.0 Results

3.1 Effect of p_{CO2}

169 The total mass loss values and average corrosion rates of 3Cr steels at 2.7 and 28.5 bar of p_{CO2} at

170 200°C after 5, 20, 48, and 120 hours of exposure are provided in Figure 3. The results indicate that

171 3Cr steel has the highest corrosion rates of 2.86 and 7.67 mm/year in the first 5 hours for 2.7 and

172 28.5 bar CO_2 partial pressure, respectively. The high corrosion rates in the first 5 hours suggest the

173 fast dissolution of the metal ions from the 3Cr matrix. The average corrosion rates gradually decline

174 over time, reaching 0.26 and 0.33 mm/ year after 120 hours for 2.7 bar and 28.5 bar of p_{CO2}

175 respectively.

176 The slowly increased mass losses between 5 hours and 20 hours result in a sharp drop of the initial

177 corrosion rates, suggesting the corrosion product scales formed on the surface and protected the

178 3Cr surface from the corrosion. The mass loss for 3Cr gradually was recorded from 12.83 to 27.88

179 g/m² between 5 hours and 120 hours at 2.7 bar of p_{CO2}, but it is stable at around 35.67 g/m² under

180 28.5 bar of p_{CO2} over this period, suggesting the different protectiveness of the corrosion scales

9

181 formed on the surface at various p_{CO2}.

182
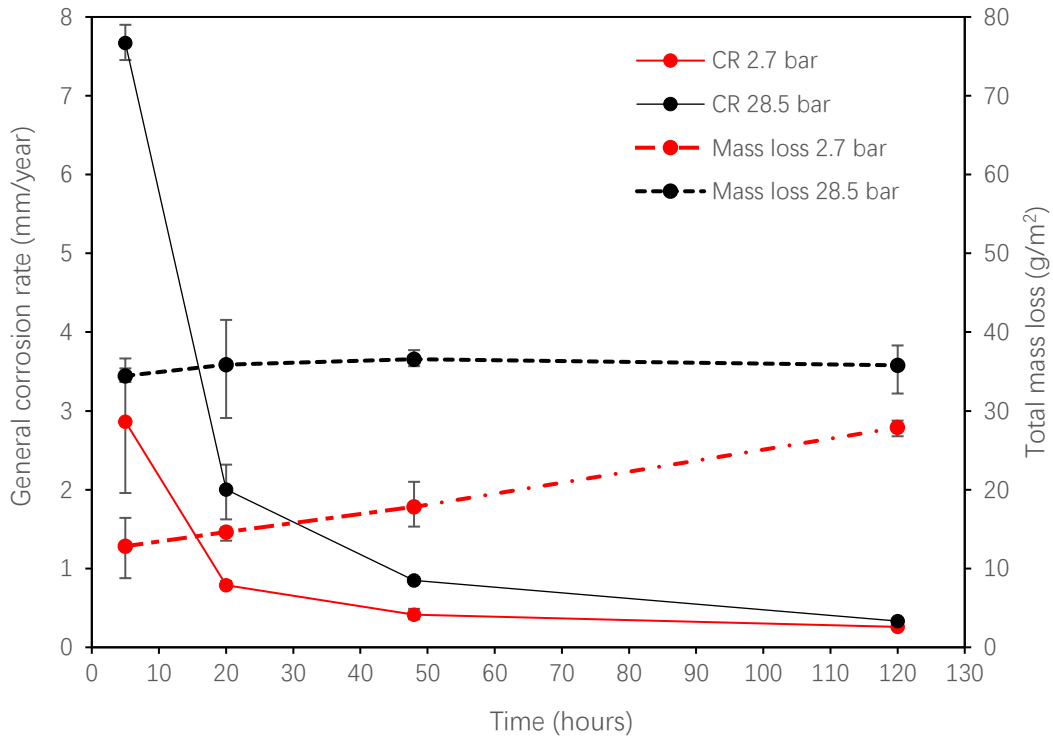
Figure 3. The total mass loss values and average corrosion rates for 3Cr steels at 2.7 and 28.5 bar

**of p_{CO2} at 200°C after 5, 20, 48, and 120 hours of exposure**

3.2 Characterisation of corrosion scales developed on the surface at both p_{CO2}

Figure 4 represents the morphology of the corrosion product scales formed on the surface after 5,

20, 48 and 120 hours. The crystals are found after 5 hours of exposure at both conditions. The

crystals at 2.7 bar of p_{CO2} are randomly distributed (Figure 4a) in comparison to the situation at p_{CO2}

of 28.5 bar where the 3Cr surface is completely covered by corrosion scales. The scatter crystals on

the surface significantly increased in number from 20 to 48 hours at 2.7 bar of CO_2 (Figure 4 c and

e), followed by increasing in size after 120 hours as shown in Figure 4g.

Under the high p_{CO2} of 28.5 bar, in-complete surface coverage was observed after 5 hours of

exposure, gaps between the corrosion scales were found. 3Cr surface is covered by dense and

10

194   compact corrosion scales after 20 hours of exposure, and there are no visible differences for the

195   corrosion product scales after generating the compact and dense scales on the surface after 20

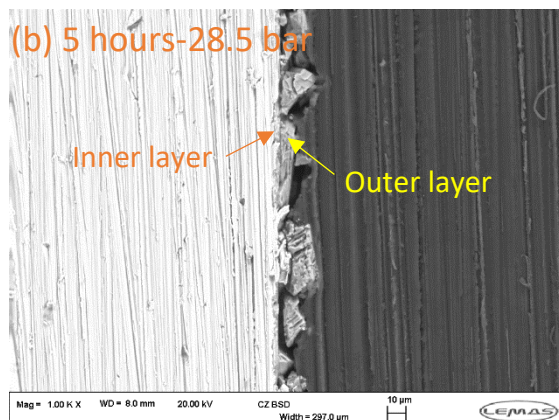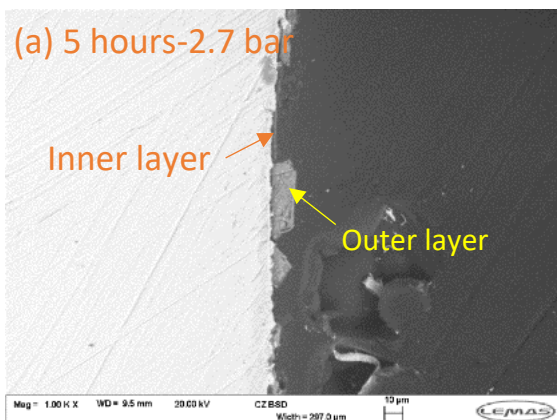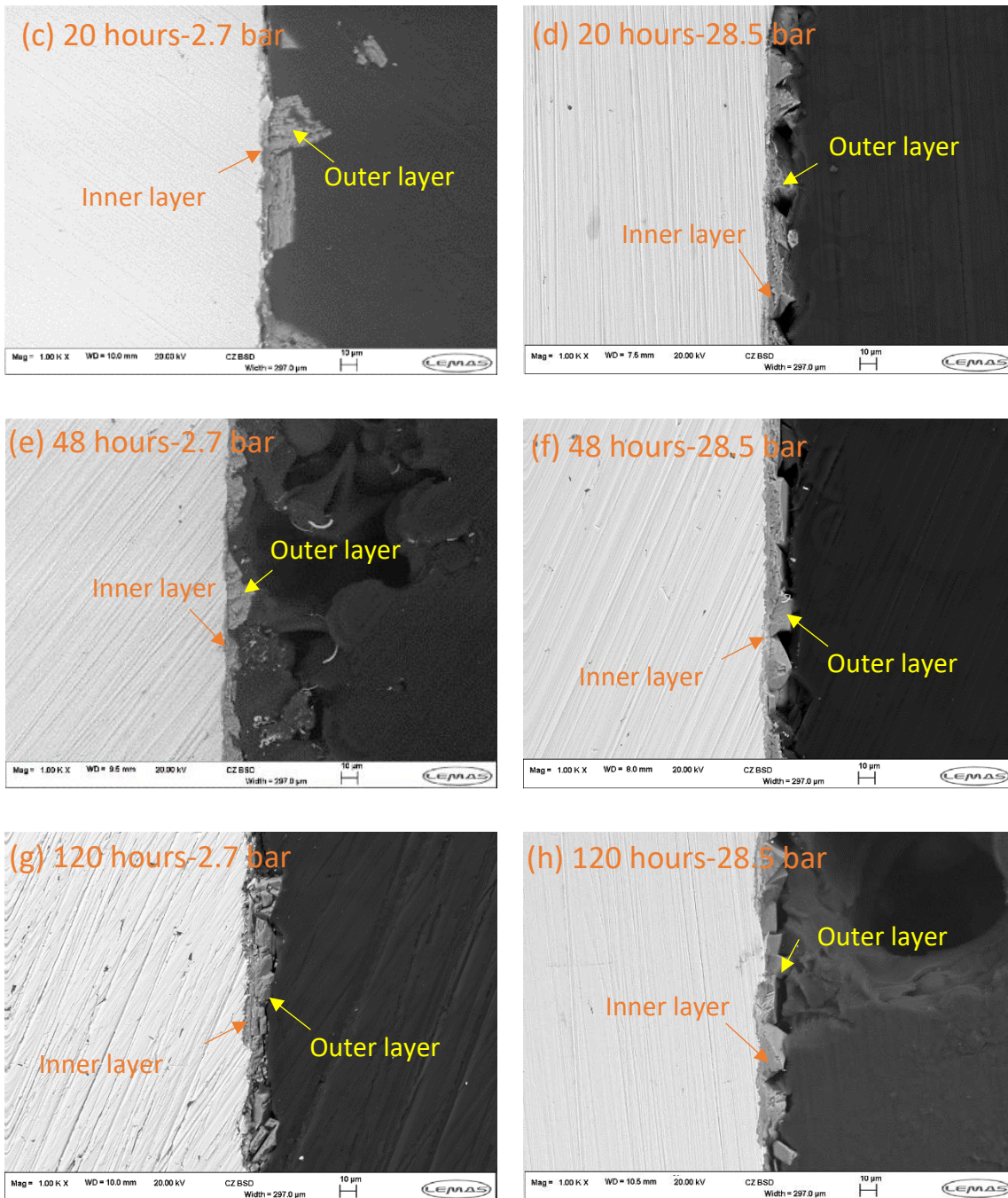196   hours as shown in Figures 4f and 4h.

(g) 120 hours-2.7 bar

(h) 120 hours-28.5 bar
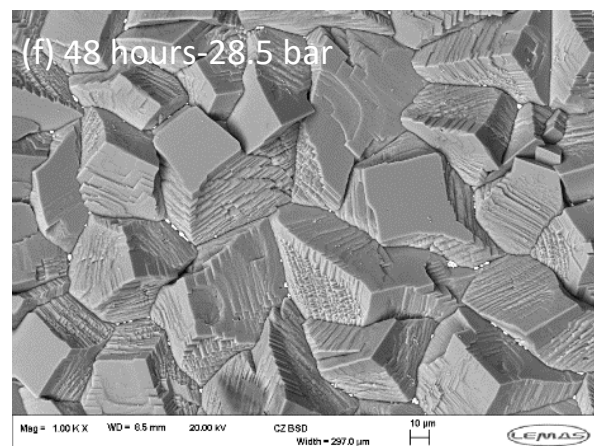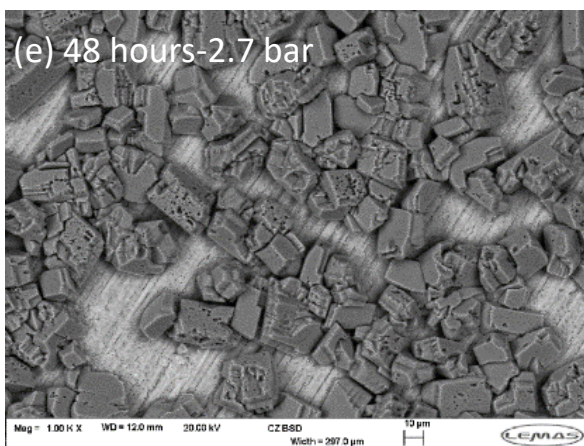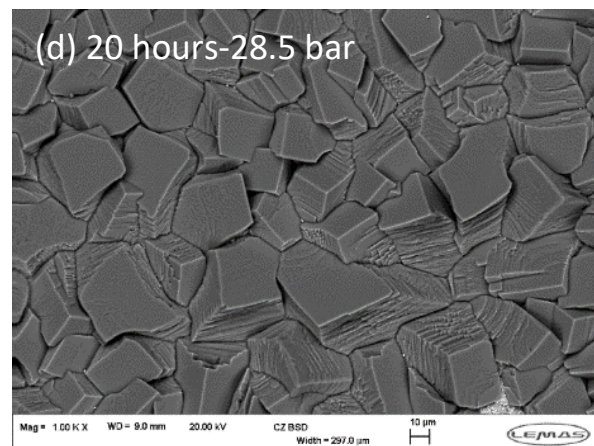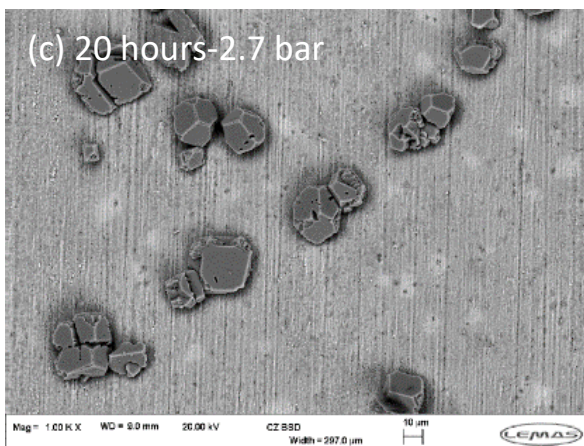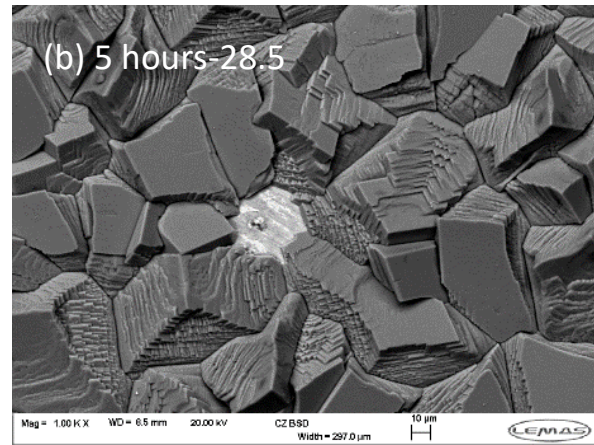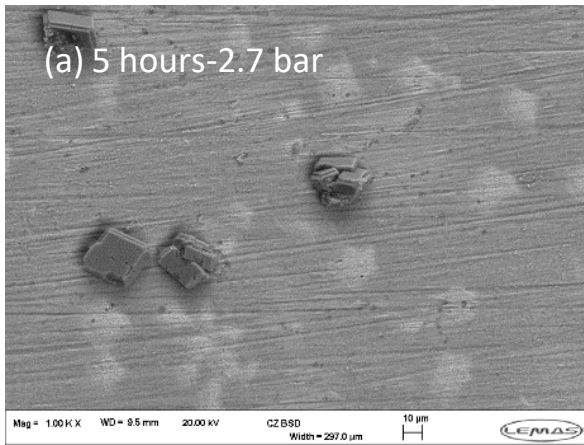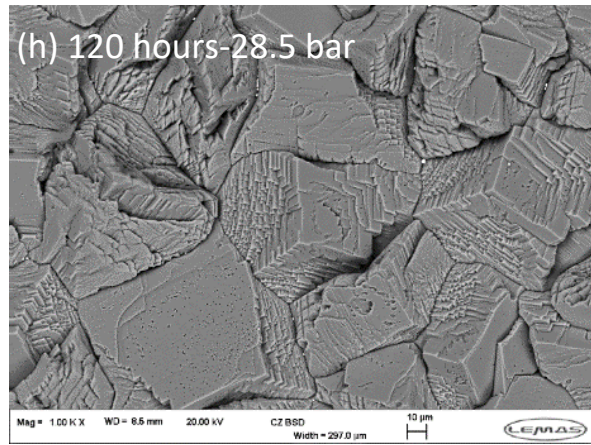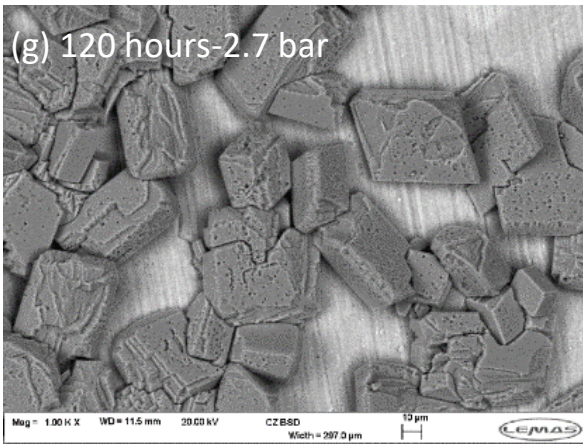
Figure 4. Surface morphology of 3Cr steels at 200°C under different p_{CO2} with different immersion time.

In Figure 5, the cross-section SEM images of corrosion product scales formed at p_{CO2} of 2.7 bar and 28.5 bar and different immersion times are presented. For 2.7 bar p_{CO2}, the outer crystals are found after 5 hours of exposure while the inner layer is thin and approximately around 1μm. After 20 hours, the thickness of the inner layer increased locally to 2-3 μm. The inner corrosion layer is non-uniformly developed over the immersion time.

For 28.5 bar p_{CO2}, the inner corrosion film is distributed non-uniformly with a thickness range between 0.1 and 5 μm over the various immersion times.


(a) 5 hours-2.7 bar
Inner layer
Outer layer

(b) 5 hours-28.5 bar
Inner layer
Outer layer

Figure 5. Cross-section images of 3Cr steel at 200°C under different p_{CO_2} with different immersion time.

Figure 6 illustrates the elemental distribution for the double-layered scales formed on 3Cr steel after 20 hours and 120 hours of exposure at 200°C and 2.7 bar of CO_2. The outer crystalline layer is comprised of Fe, O and C compounds and precipitated on a Cr-enriched inner layer. It can be seen

13

that the high chromium content accumulated at the matrix/inner layer interface after 20 hours and
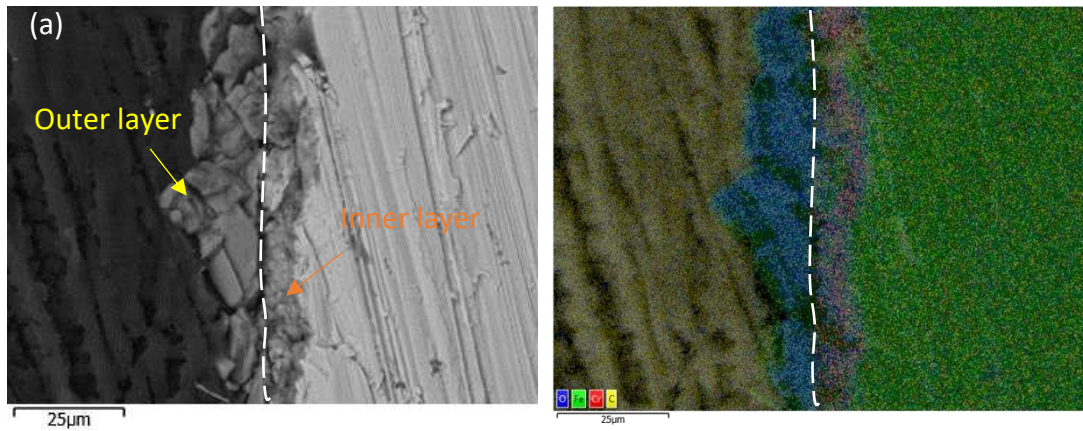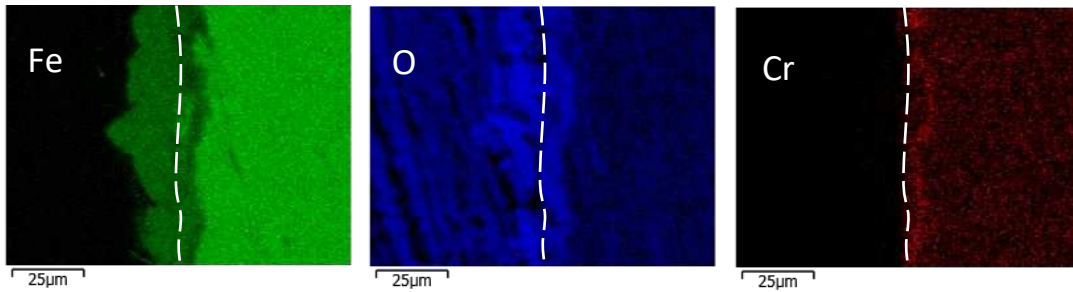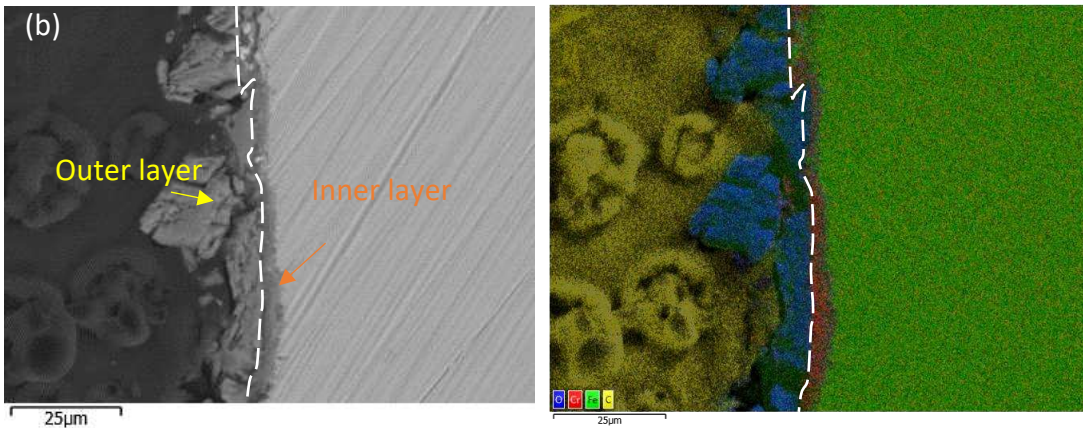
120 hours.

Figure 6. Elemental distribution of double-layered scale formed on 3Cr steel in (a) 20 hours and

(b) 120 hours at 200°C and 2.7 bar p_{CO_2}.

A similar Cr-rich inner layer was detected on the 3Cr steel surface at 200°C and 28.5 bar of p_{CO_2} as

shown in Figure 7. A high concentration of Cr layer was observed throughout the inner layer after

20 hours. The development of the outer layer becomes uniform and the overall thickness of the

corrosion product layers is 20-25 µm over 120 hours of exposure.
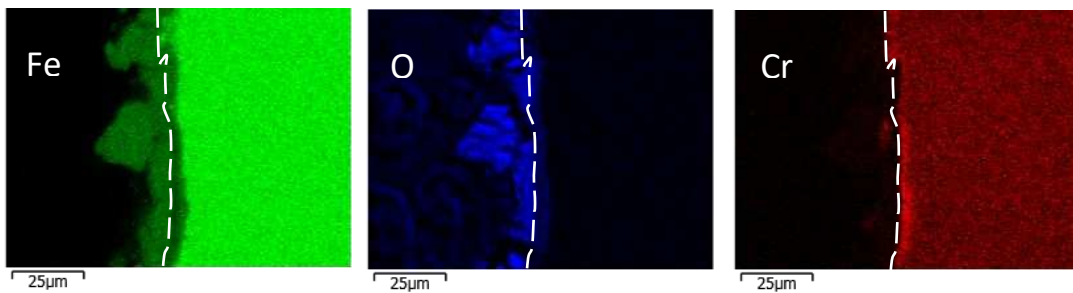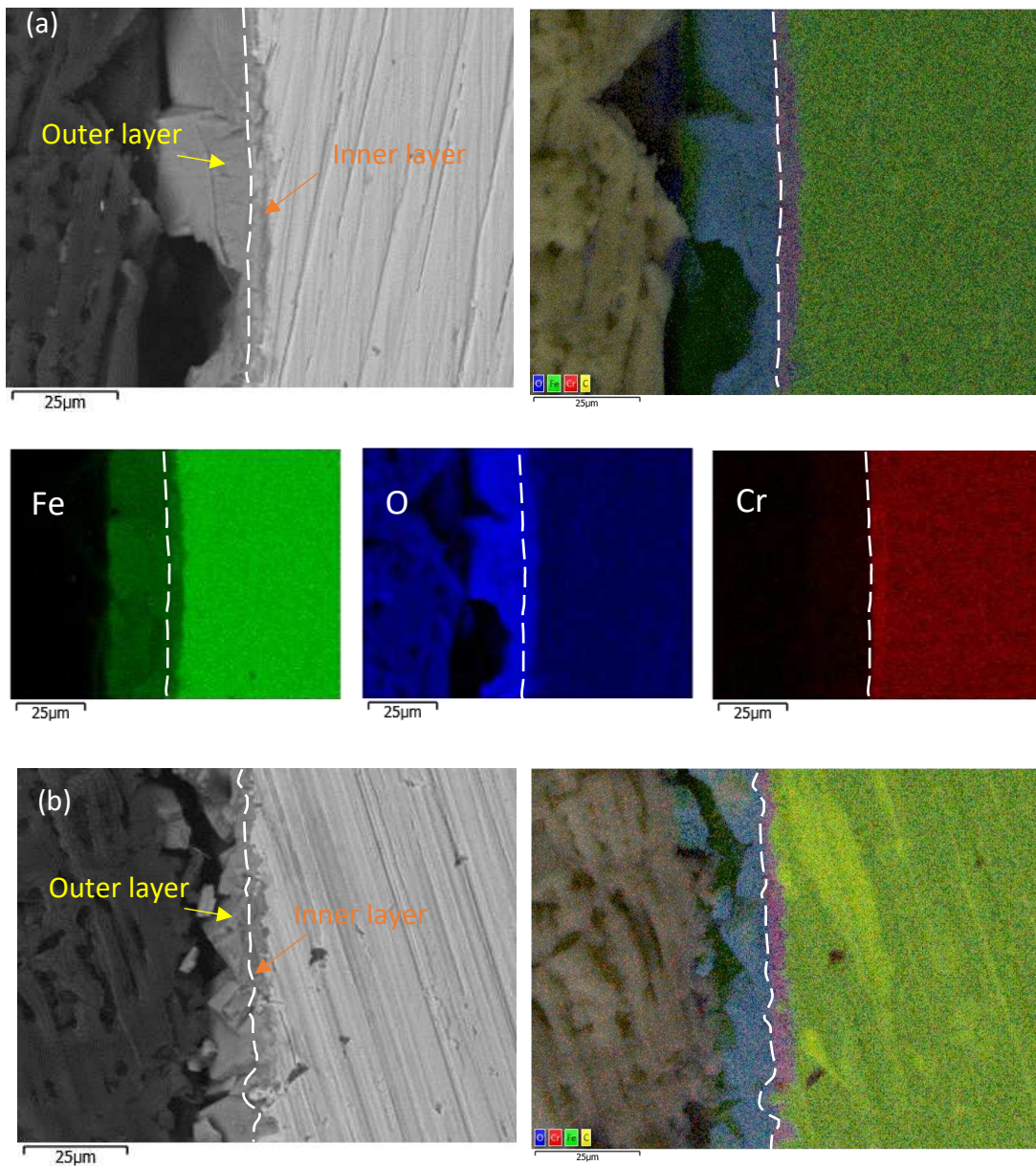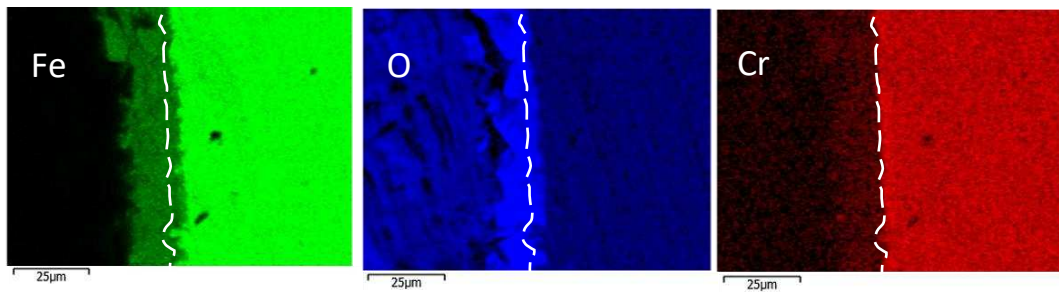

15

Figure 7. Elemental distribution of double-layered scales formed on 3Cr steel in (a) 20 hours and (b) 120 hours at 200°C and 28.5 bar p_{CO2}.

A combination of Raman spectroscopy and XRD was employed to determine the composition of the corrosion scales developed on the steel surface at various immersion times. Fig. 8 shows the XRD patterns of the corrosion scales formed on the surface for both p_{CO2}, highlighting that the detected dominant crystalline phase on the steel surface is $FeCO_3$. In Figure 8a, it is interesting to note that the intensity of the Fe peak located at 44.5° decreased with the enhanced $FeCO_3$ peaks (are located at 24.8° and 32.1°) as the exposure time is prolonged. The results suggest that the thickness of the crystalline $FeCO_3$ increased via the precipitation processes at p_{CO2} of 2.7 bar. Moreover, a peak located at around 35.5° is detected which belongs to a spinel structure at various immersion times. Previous studies reported that the peak at 35.5° is typical spinel (Fe_3O_4 or $FeCr_2O_4$)[21]. However, the indistinguishable diffraction peaks for these corrosion scales require further tests to determine the composition.

As the p_{CO2} increased to 28.5 bar, only $FeCO_3$ and Fe peaks were detected on the surface as shown in Figure 8b and the peak intensities show no differences at various immersion times.

16

242

243
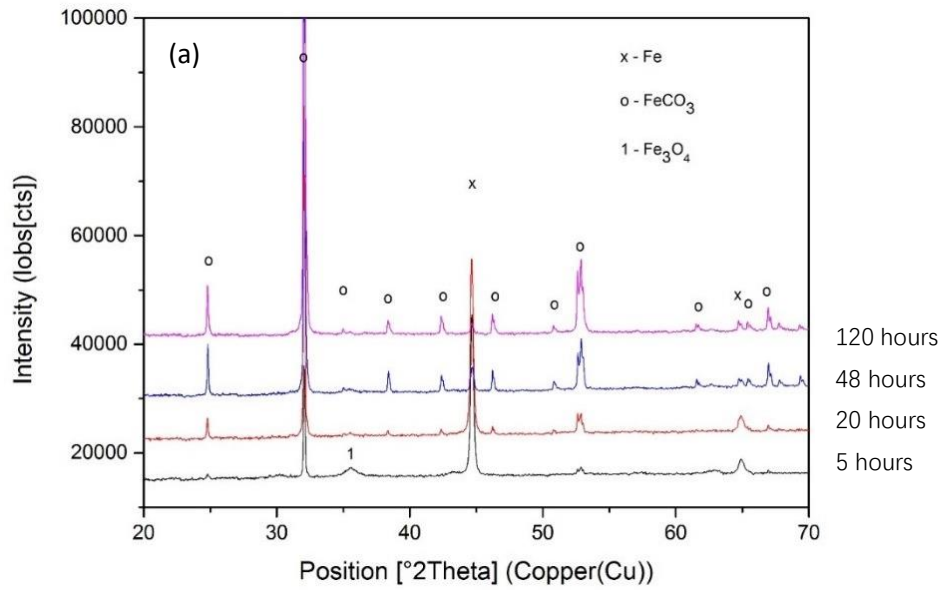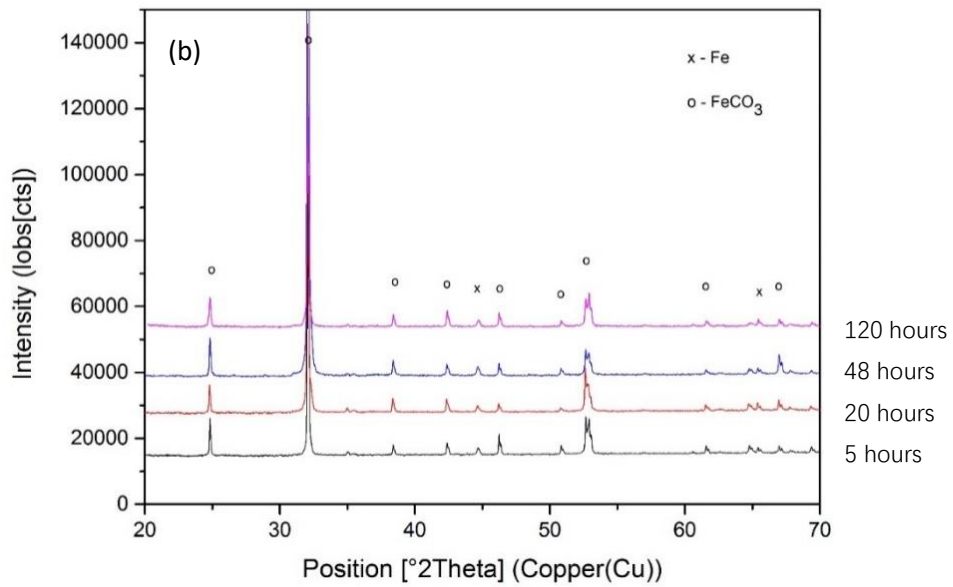
Figure 8. XRD of 3Cr steel with different immersion times at 200°C, (a) 2.7 bar and (b) 28.5 bar

p_{CO2}.

The Raman spectra for samples exposed to the CO_2-saturated solution at various immersion times are provided in Figure 9. For 2.7 bar p_{CO2}, the results in Figure 9a indicate that the precipitation of the outer $FeCO_3$ crystals is located at 1086 cm^{-1} and the inner Fe_3O_4 layer is at 667 cm^{-1} from 5 to 48 hours of exposure. It is interesting to note that the peak is located at 667 cm^{-1} becoming wider after 48 hours and implies the formation of the mixed compounds for the inner layer over longer

17

251   immersion times. The local Raman spectra was measured via the cross-section as shown in Figure

252   9a confirmed that the inner layer contains $FeCr_2O_4$ and $Cr(OH)_3$ after 120 hours, which in agreement

253   with EDS measurements that a rich-Cr inner layer is detected as shown in Figure 6.

254   For the corrosion product scales formed on the surface at 28.5 bar of CO_2 (Figure 9b), similar to the

255   results for 2.7 bar of p_{CO2}, the double-layered scales are comprised of a $FeCO_3$ outer layer and the

256   inner layer insisting of both $Cr(OH)_3$ and $FeCr_2O_4$.
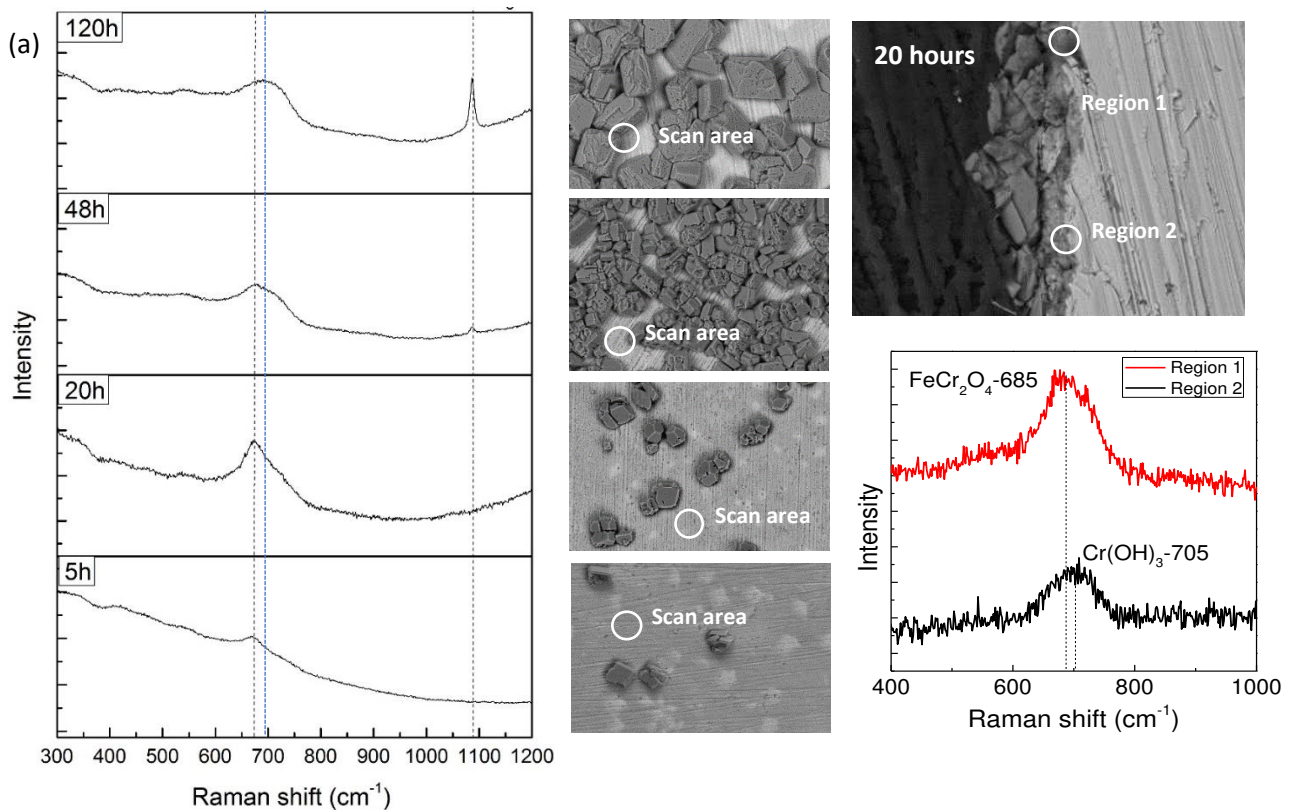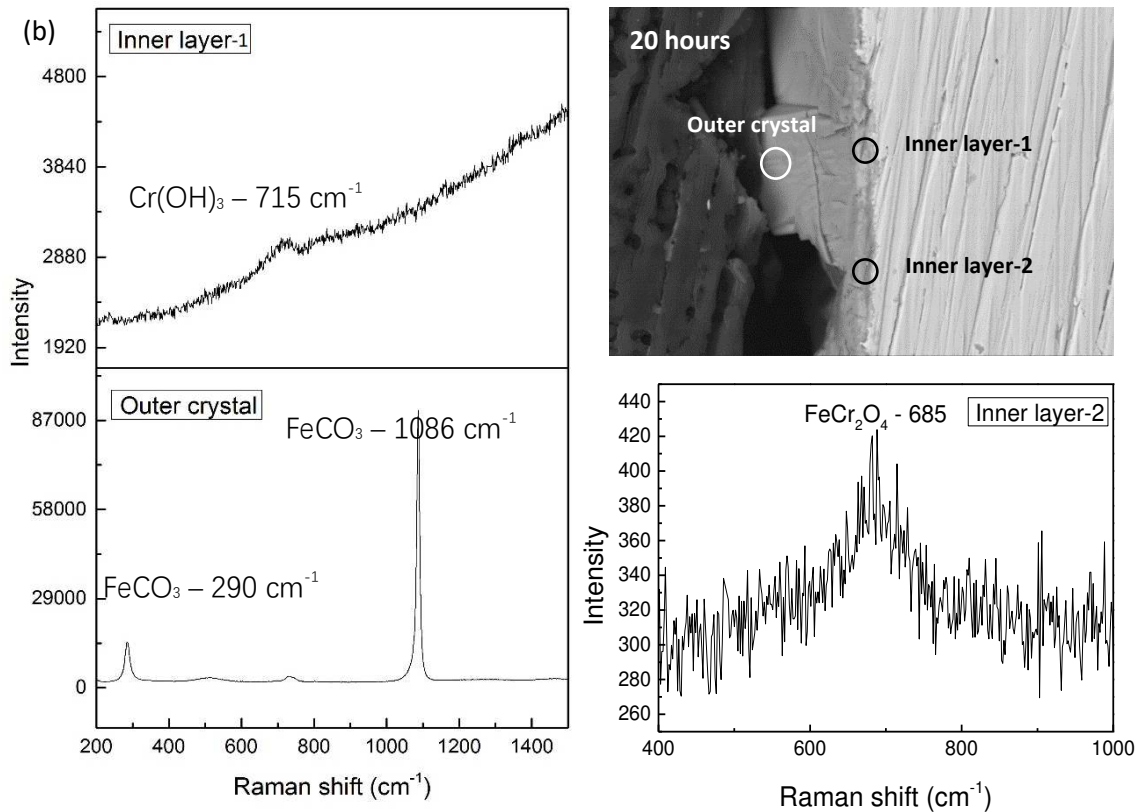
Figure 9. Raman spectra of 3Cr steel with different immersion time at 200°C and (a) 2.7 bar CO_2, (b) 28.5 bar CO_2.

3.3 Localised corrosion behaviour of 3Cr steels immersed to the CO_2-saturated solution at p_{CO2} of 2.7 and 28.5 bar

After the removal of the corrosion scales from the surface according to ASTM G 01-03[19], profilometry was performed on the surface and the average pitting depths were calculated by considering the top 10 deepest pits from each sample. The results are provided in Figure 10. For p_{CO2} of 2.7 bar, the average pit depth increased from 2.5 to 5.3 μm between 5 and 120 hours; this suggests that the pits grow slowly at low p_{CO2}. Conversely, an average pitting depth of 11.6 μm was measured after 5 hours at the condition of 28.5 bar p_{CO2}, and it increased slightly to 13.4 μm after 20 hours. The pit depth maintains relatively stable at approximately 13.7 μm after 120 hours with the formation of the double-layered corrosion product scales on the surface.

19

270   The examples of 2D profilometry images of 3 mm x 3 mm scanned areas from the 3Cr surface are

271   provided in Figure 10. The results exhibit that 3Cr suffers a higher localised corrosion attack at 200°C

272   and 28.5 bar p_{CO2} compared to low p_{CO2} of 2.7 bar. There is no obvious development of the localised

273   corrosion attack over the immersion time at 2.7 bar. However, the increased p_{CO2} from 2.7 bar to

274   28.5 bar, resulting in the level of localised attack is 5 times higher and suggests that the localised

275   corrosion rates become severe with increasing p_{CO2}.

276

277

278

279

280
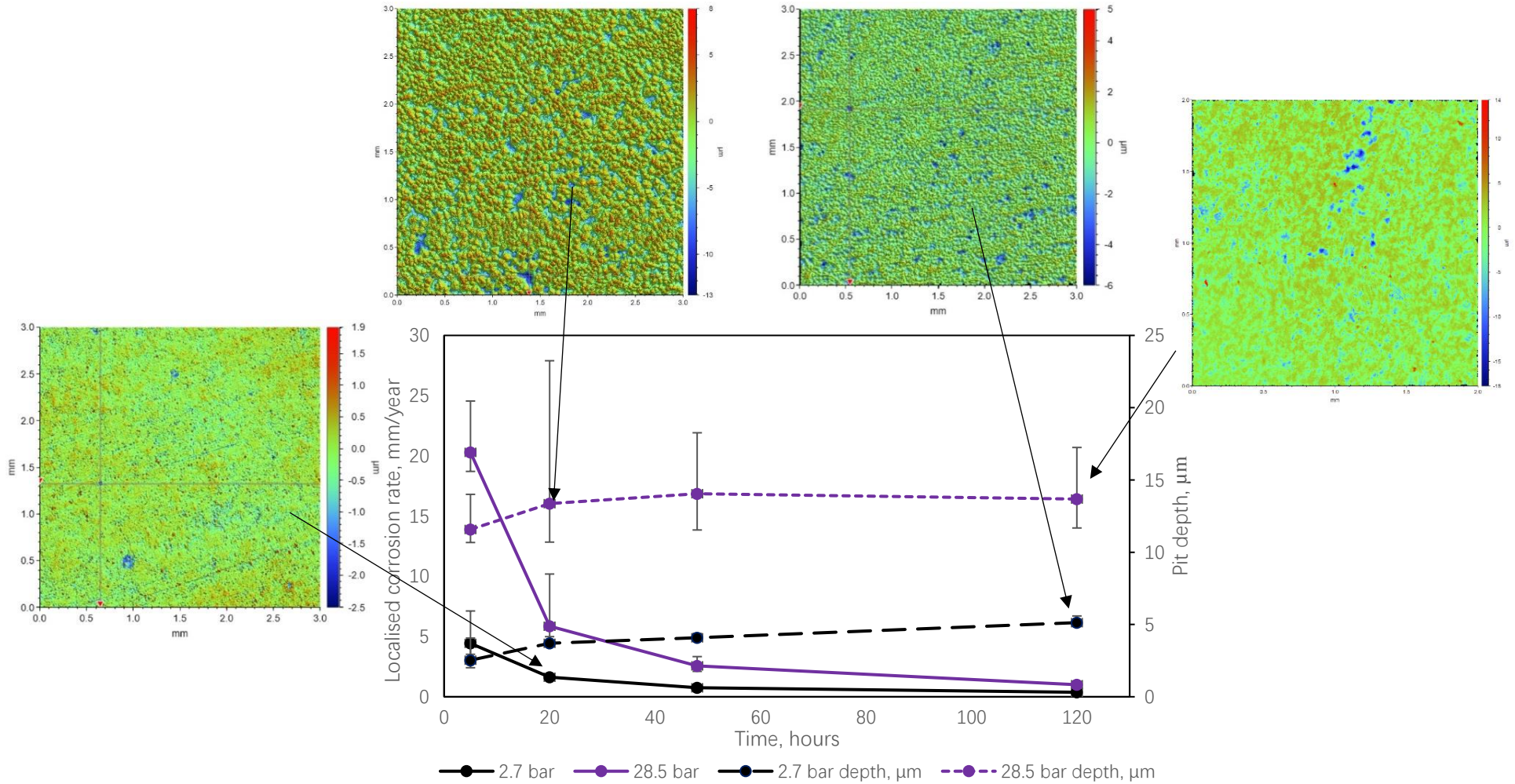
Figure 10. Profilometry of 3Cr steel after 5, 20, 48 and 120 hours of exposure at 200°C and p_{CO2} of 2.7 and 28.5 bar respectively.

282   Figure 11 shows the surface morphology of the sample after the removal of the corrosion

283   scales. As shown in Figure 11 a and c, localised/pitting was observed on the surface after 5

284   and 20 hours of exposure at p_{CO2} of 2.7 bar. The pits on the surface develop onto large and

285   wide localised corrosion over-long immersion periods as shown in Figure 11 g. For the 28.5

286   bar of p_{CO2}, the pits are randomly distributed on the surface in the early stages. It can be seen

287   that the sample surface suffers localised attack over long-term exposure.
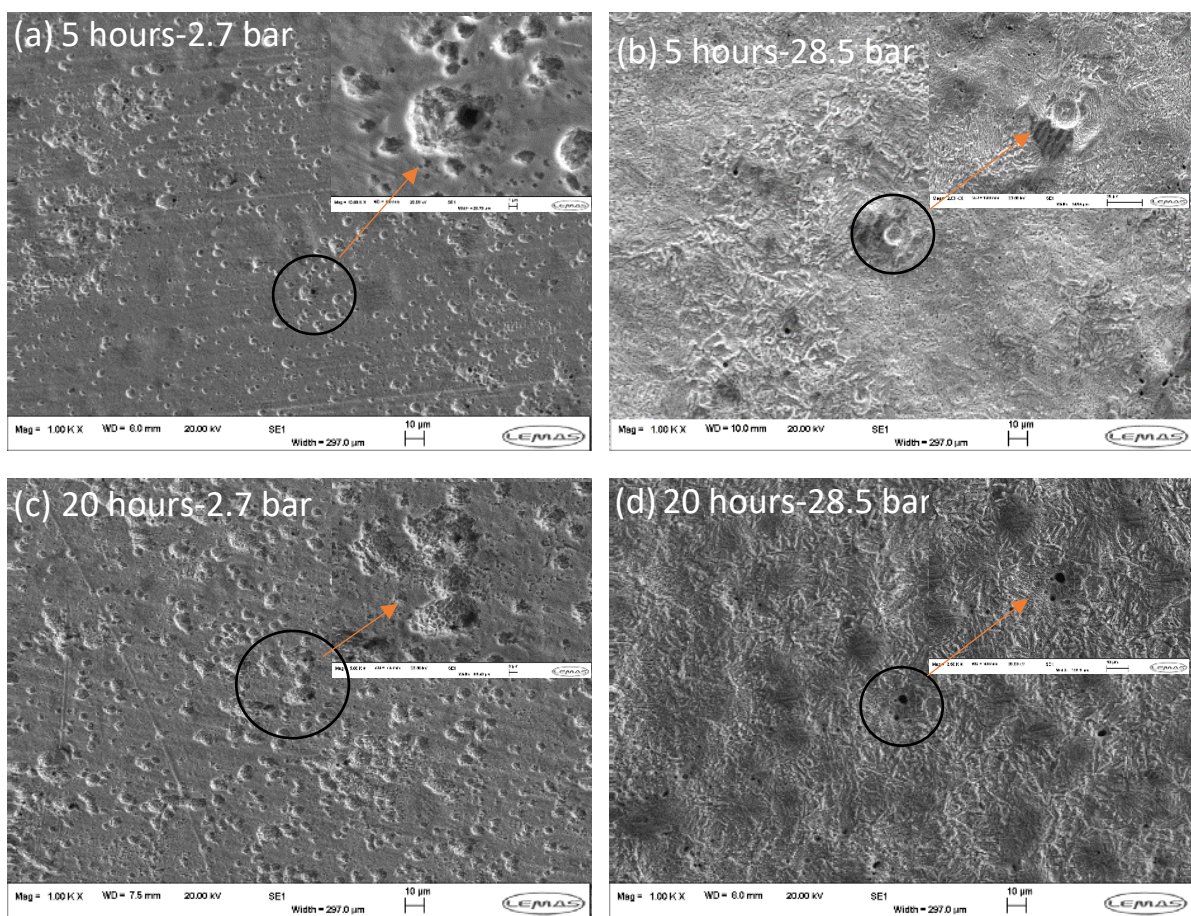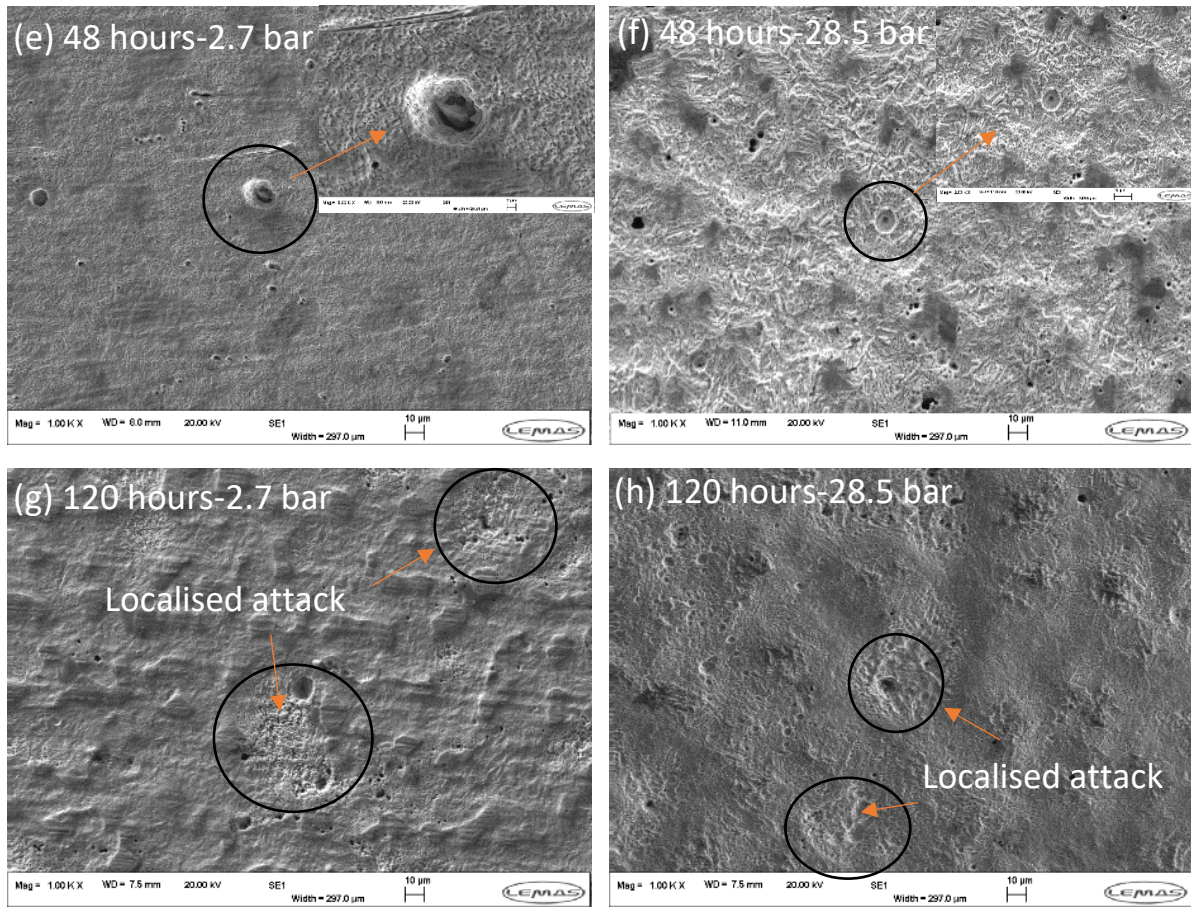
Figure 11. SEM images of 3Cr steel after removing corrosion scales after 5, 20, 48 and 120 hours of exposure at 200°C and p_{CO2} of 2.7 and 28.5 bar.

3.4 Characterisation of the localised corrosion and inner corrosion layer at steel interface

To further understand the correlation between the measured localised corrosion and the corrosion product scales formed on the 3Cr surface, FIB combined with high-resolution SEM and EDS were applied. The cross-section prepared by FIB provides the analysis region of the corrosion scales formed on the surface at 200°C and 2.7 bar of p_{CO2} as shown in Figure 12. Figure 12b exhibits the inner layer is approximately 1 μm in thickness, and it covered the entire surface including the areas beneath the outer crystalline $FeCO_3$, suggesting good general corrosion protection to the steel surface (Figure 3). However, the localized/pits were

23

298   observed at the matrix/inner layer interface in regions 1 and 2 (Figure 12b). The line-scans in

299   regions 1 and 2 show no obvious Cl$^-$ ion distributed in the inner layer, indicating a relatively

300   mild localised corrosion for 3Cr steel at 200°C and 2.7 bar of p_{CO2} without the acceleration by

301   Cl$^-$, consistent with the observation of the localised corrosion shown in Figure 11.

302

303
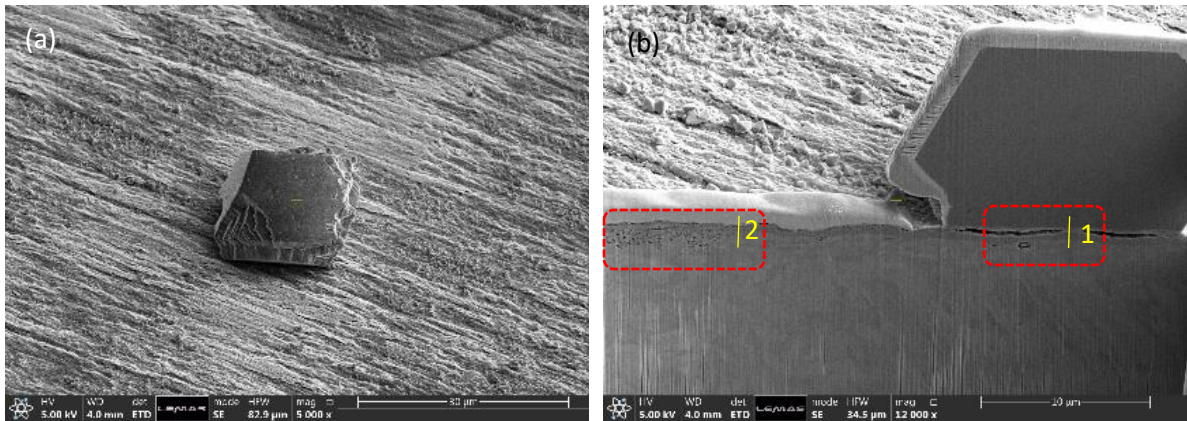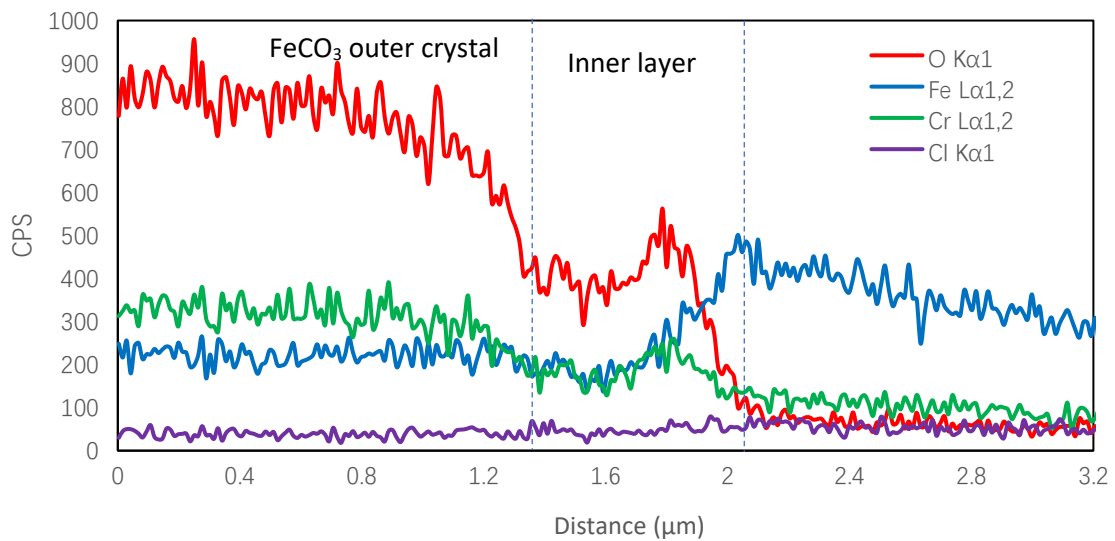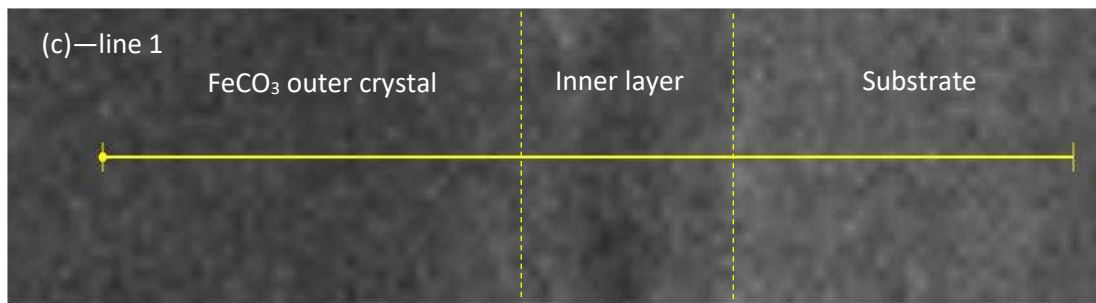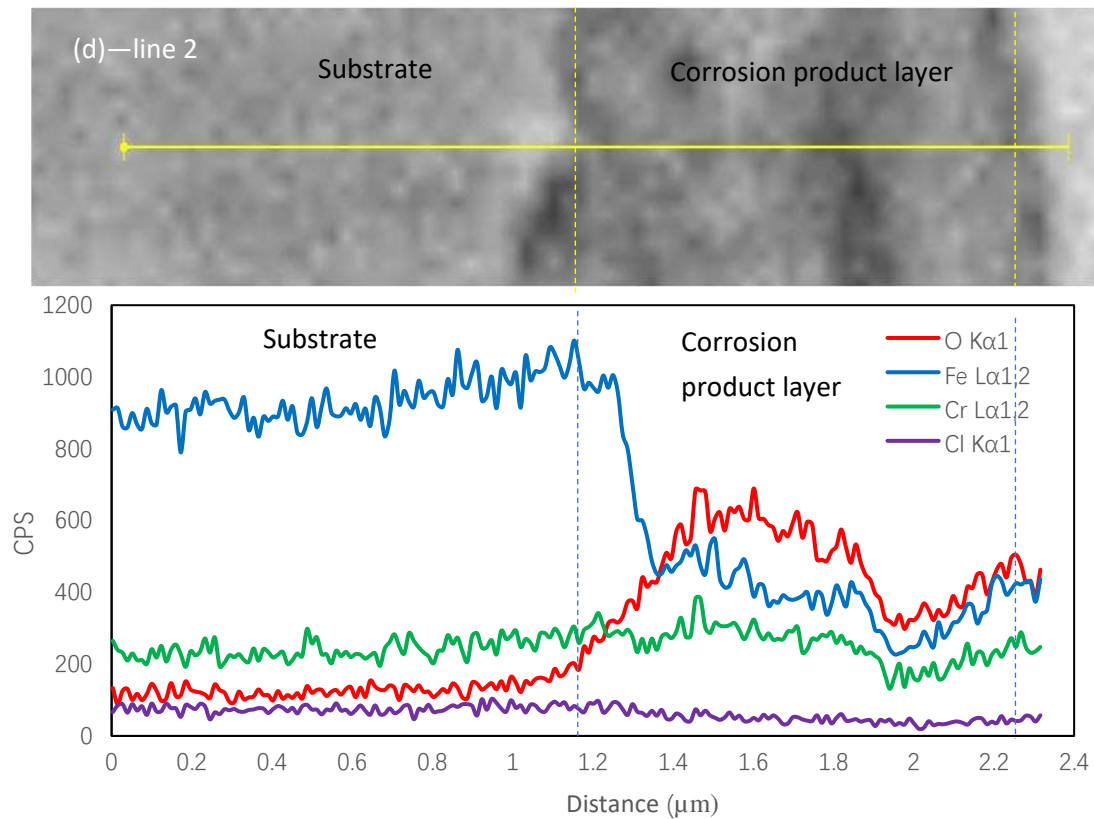
Figure 12. SEM images of analysis region (200°C and 2.7 bar p_{CO2} sample) after 20 hours, showing (a) where ion milling was performed, (b) the cross-section milled away within the surface, and EDS line-scans from (c) line-1 and (d) line-2.

Figure 13 provides the analysis region of the corrosion scales for the samples immersed in the solution at 28.5 bar of p_{CO2} and the sample was prepared via FIB. Figure 13b shows that the inner layer appears to be non-uniform, approximately between 1 and 5 μm. The localised/pitting was observed at the matrix/inner layer interface. The line-scan as shown in Figure 13c indicates that a high Cl⁻ concentration is contained within the inner layer, suggesting that the defects of the inner layer cause the Cl⁻ ions easily to penetrate, resulting in high localized corrosion occurred on the surface.

315

316

317
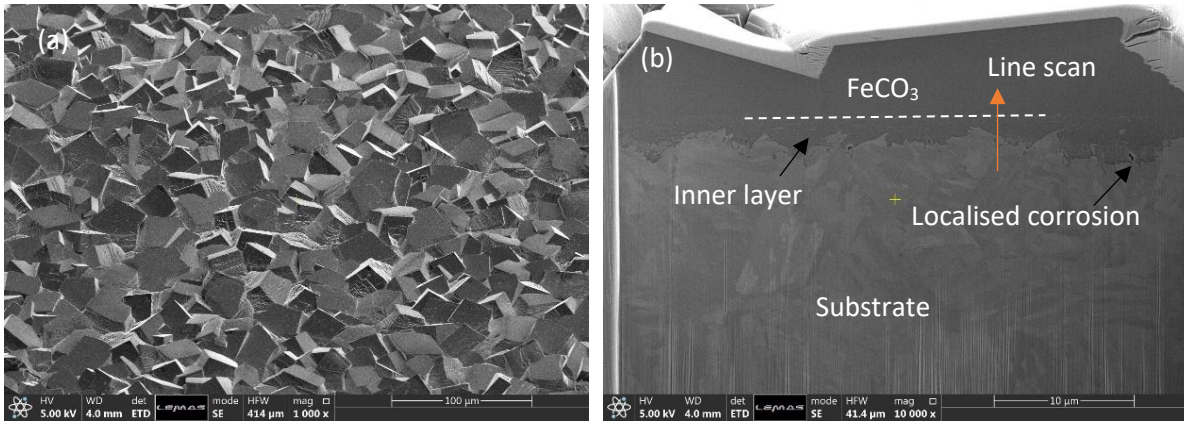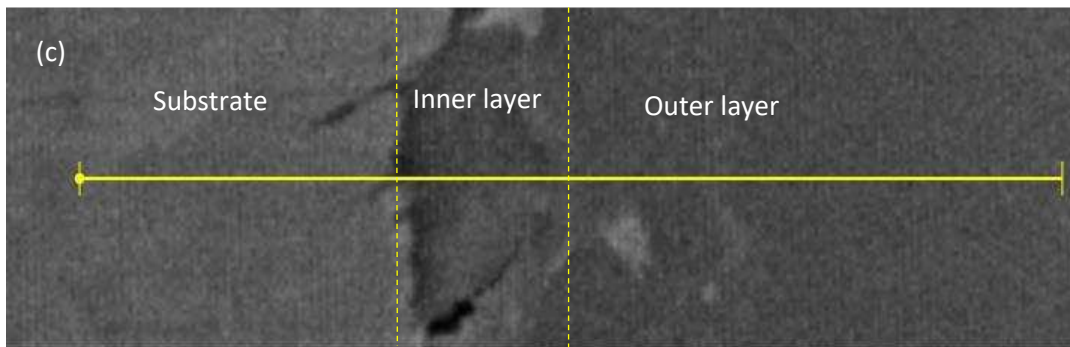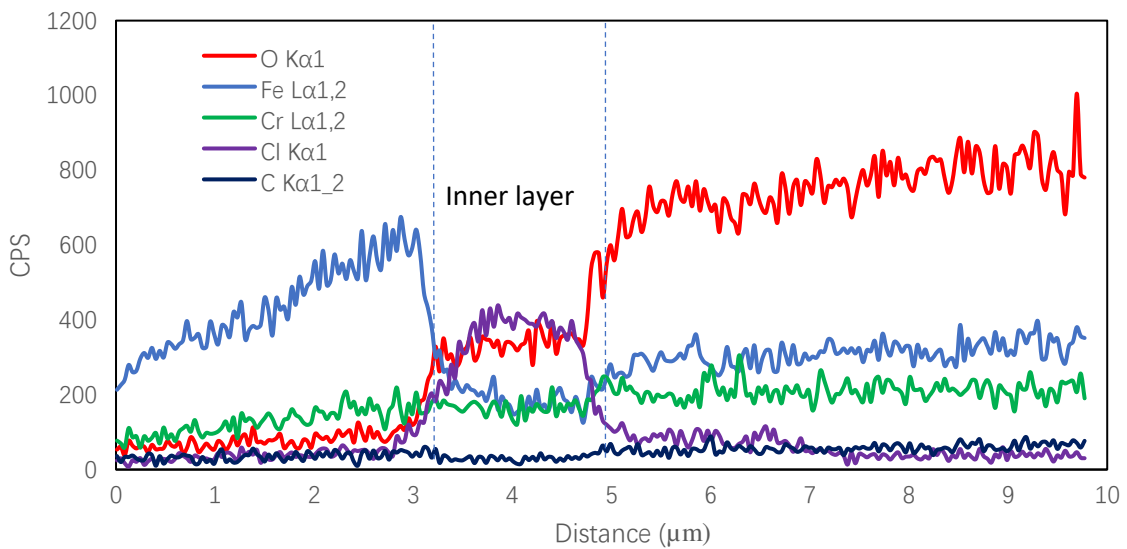
Figure 13. SEM images of analysis region (200ºC and 28.5 bar p_{CO2} sample) after 20 hours,

318

showing (a) where ion milling was performed, (b) the cross-section milled away within the

319

surface, and (c) EDS line-scan.

320

321

322 **4.0 Discussion**

323 **4.1 The compositions of double-layered corrosion scales for 3Cr at 2.7 bar of p_{CO2}**

324 **4.1.1 The development of the double-layered corrosion scales for Fe-H$_2$O-CO$_2$-Cl$^-$ system at**

325 **200°C and 2.7 bar p_{CO2}**

326 To reveal the formation of the double-layered corrosion scales on the 3Cr surface exposed to

327 the CO$_2$-saturated solution at various p_{CO2} values for a constant temperature of 200°C,

328 Pourbaix diagrams were employed to ascertain the various thermodynamically stable

329 corrosion scales formed on the surface. Considering the relative low Cr concentration within

330 the system since Fe is the major contributed dissolution ion in the early stage, Figure 14

331 illustrates the constructing Pourbaix diagram for 2.7 bar p_{CO2} conditions at 200°C for the Fe-

332 H$_2$O-CO$_2$-Cl$^-$ systems, where the red and purple represent solid and aqueous phases,

333 respectively. The detected corrosion scales by XRD and Raman spectra confirmed that the

334 corrosion scales are mainly comprised of a Fe$_3$O$_4$ inner layer and the outer FeCO$_3$ layer at 2.7

335 bar of p_{CO2} and 200°C after 5 hours of exposure, which is consistent with the constructing

336 Pourbaix diagram. The potential anodic processes for the dissolution and the solid-phase

337 formation at the surface of 3Cr steel [30, 31]:

$$Fe \leftrightarrow Fe^{2+} + 2e^- \tag{2}$$

$$3Fe^{2+} + 4H_2O \leftrightarrow Fe_3O_4(s) + 8H^+(aq) + 2e^- \tag{3}$$

$$Fe(s) + H_2CO_3(aq) + \leftrightarrow FeCO_3(s) + 2H^+(aq) + 2e^- \tag{4}$$

$$3FeCO_3(s) + 4H_2O \leftrightarrow Fe_3O_4(s) + 3H_2CO_3(aq) + 2H^+(aq) + 2e^- \tag{5}$$

27
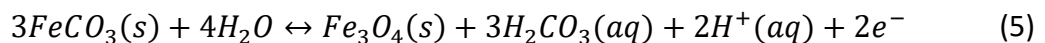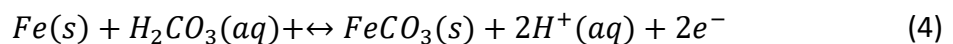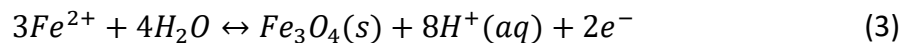
338   The thermodynamic equilibrium electrode potential for the above reactions is presented as

339   follows and marked as boundary lines in Figure 14.

$$E_{Fe^{2+}/Fe} = E^0_{Fe^{2+}/Fe} + \frac{2.3RT}{nF} lg c_{Fe^{2+}} \cdots\cdots\cdots line \; ① \qquad (6)$$

$$E_{Fe_3O_4/Fe^{2+}} = E^0_{Fe_3O_4/Fe^{2+}} + \frac{2.3RT}{nF} lg \frac{c^8_{H^+}}{c^3_{Fe^{2+}}} \cdots\cdots\cdots line \; ② \qquad (7)$$

$$E_{Fe/FeCO_3}(pH < 7.17) = E^0_{Fe/FeCO_3} + \frac{2.3RT}{2F} lg \frac{c^2_{H^+}}{c_{H_2CO_3}} \cdots\cdots\cdots line \; ③ \qquad (8)$$

$$E_{FeCO_3/Fe_3O_4} = E^0_{FeCO_3/Fe_3O_4} + \frac{2.3RT}{2F} lg c^2_{H^+} \cdot c^3_{H_2CO_3} \cdots\cdots\cdots line \; ④ \qquad (9)$$

340   In the early stage, ferrite ions are preferentially dissolved via reaction (2) and this suggests

341   the development of Fe_3O_4 via crossing boundary ①-② at the pH below 6.38. The inner layer

342   continuously forms and simultaneously dissolves by the equilibrium reaction (3). The ferrous

343   ions stay thermodynamically stable in the aqueous phase (pH<6.94), indicating the

344   consumption of the inner layer and a relatively high corrosion rate at this stage.

345   The development of the corrosion scales at the solution/inner layer interface leads the

346   cathodic reactions consuming acidity via as follows:

$$2H^+(aq) + 2e^- \leftrightarrow H_2(g) \qquad (10)$$

$$2H_2CO_3(aq) + 2e^- \leftrightarrow 2HCO_3^-(aq) + H_2(g) \qquad (11)$$

$$2HCO_3^-(aq) + 2e^- \leftrightarrow 2CO_3^{2-}(aq) + H_2(g) \qquad (12)$$

$$2H_2O + 2e^- \leftrightarrow 2OH^-(aq) + H_2(g) \qquad (13)$$

28
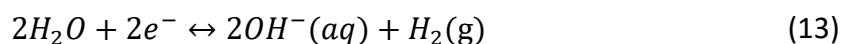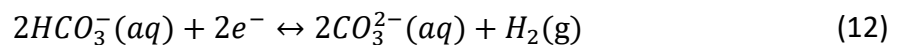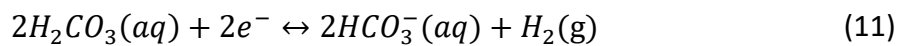
347 The increase in solution pH, shifting the thermodynamic region to the $FeCO_3$ region in the

348 aqueous phase. At this stage, $FeCO_3$ replaces ferrous ions and coexists with Fe_3O_4. For the

349 prolonged time, the observation of the outer $FeCO_3$ crystals over 5 hours at 2.7 bar p_{CO2}

350 (Figure 4) verify the precipitation of $FeCO_3$ which nucleates after the supersaturation (*SR*)

351 exceeding a critical value (*SR*critical):

$$SR = \frac{[Fe^{2+}][CO_3^{2-}]}{K_{SP}} \geq SR_{critical} \tag{14}$$

352 Where $[Fe^{2+}]$ is the concentration of Fe^{2+}, $[CO_3^{2-}]$ is the concentration of CO_3^{2-}, and K_{SP} is

353 the solubility product for $FeCO_3$[27].

354 The scattered $FeCO_3$ increases in number between 5 hours and 48 hours which corresponds

355 to a relatively high *SR*; it increases in size over 120 hours, corresponding to the decrease of

356 *SR*. The declination of *SR* indicates the improvement of the corrosion product layer against

357 Fe^{2+} diffusion, suggesting the inner layer that coexists with $FeCO_3$ is protective of the steel

358 surface, consistent with the results proposed by Hua et al. [17]. However, the development of

359 $FeCO_3$ processes is via kinetics, Pourbaix diagram is considered the thermodynamic which is

360 the limitation for this system.
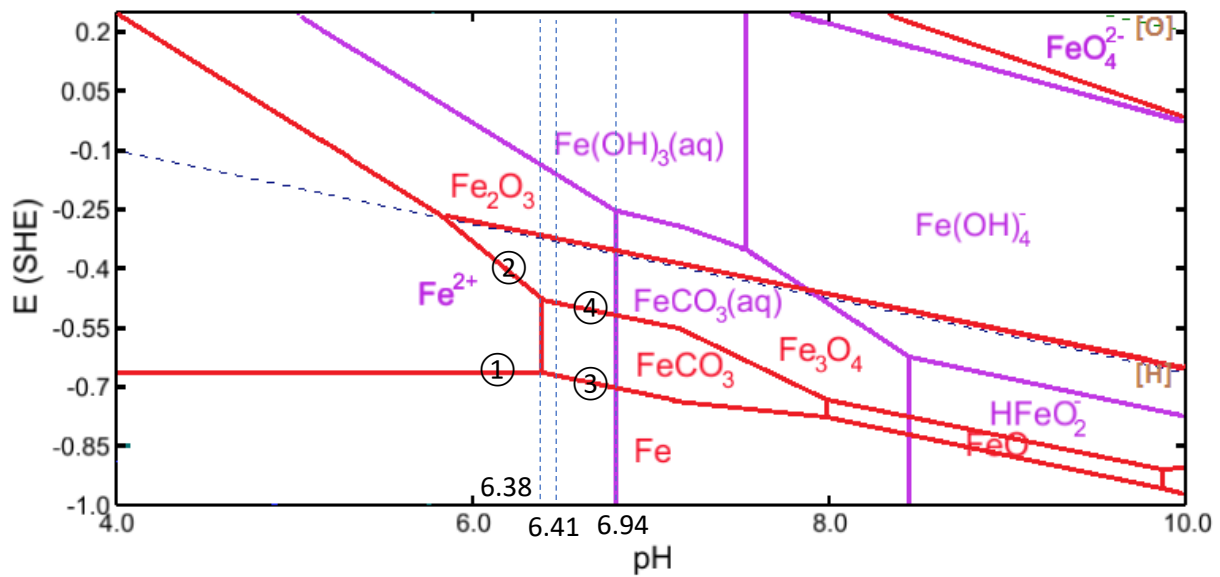
Figure 14. Pourbaix diagrams for Fe-H_2O-CO_2-Cl^- systems in the CO_2-saturated solution at 200°C and 2.7 bar p_{CO2}.

4.1.2 The development of the inner corrosion scales for the Fe-Cr-H_2O-CO_2-Cl^- systems at 200°C and p_{CO2} of 2.7 bar

The dissolution processes affect the thermodynamically stable product form on the 3Cr steel surface. [Fe^{2+}] and [Cr^{3+}] concentrations were introduced based on the mass loss of 3Cr immersed in the solution after 20 hours of exposure and simplified allocated as the elemental composition (Fe: Cr = 97 wt%: 3 wt %) for Pourbaix diagram calculation. Figure 15 illustrates the constructing Porbaix diagram for the Fe-Cr-H_2O-CO_2-Cl^- systems in comparison to the Fe-H_2O-CO_2-Cl^- systems (the calculated pH is 6.41 and corrosion potential is -0.48 V/SHE in the system) as shown in Figure 14. The Cr is considered under this circumstance due to the accumulation of Cr compounds ($FeCr_2O_4$ and $Cr(OH)_3$) during the whole corrosion processes. The formation of the spinel structure $FeCr_2O_4$ is via the reaction (15).

$$Fe(s) + 2Cr^{3+} + 4H_2O \leftrightarrow FeCr_2O_4(s) + 8H^+(aq) + 2e^-$$ (15)

30
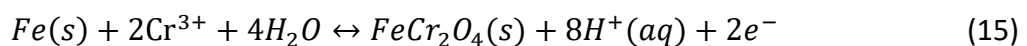
375   The Fe^{3+} sites occupy by Cr^{3+} in the spinel structure improves the film protectiveness of the

376   inner layer owing to the stronger binding energy replaced by Cr-O bond[22]. The involvement

377   of Cr in the inner layer decreases the corrosion rate as shown in Figure 3 and gradually reduces

378   the metal ion diffusion throughout the inner layer.

379   Meanwhile, the accumulation of Cr^{3+} accelerates the precipitation of $Cr(OH)_3$ within the inner

380   layer via reaction (16), which is reported as a typical compound for the Cr-bearing steels at

381   relatively low pH environments[8, 23].

$$Cr^{3+}(aq) + 3H_2O \leftrightarrow Cr(OH)_3(aq) + 3H^+ \qquad (16)$$

382   The precipitation of $Cr(OH)_3$ consumes alkalinity and results in a decrease of localised pH,

383   following by subsequently enhances matrix dissolution and accelerates the formation of

384    $FeCr_2O_4$ and $Cr(OH)_3$.
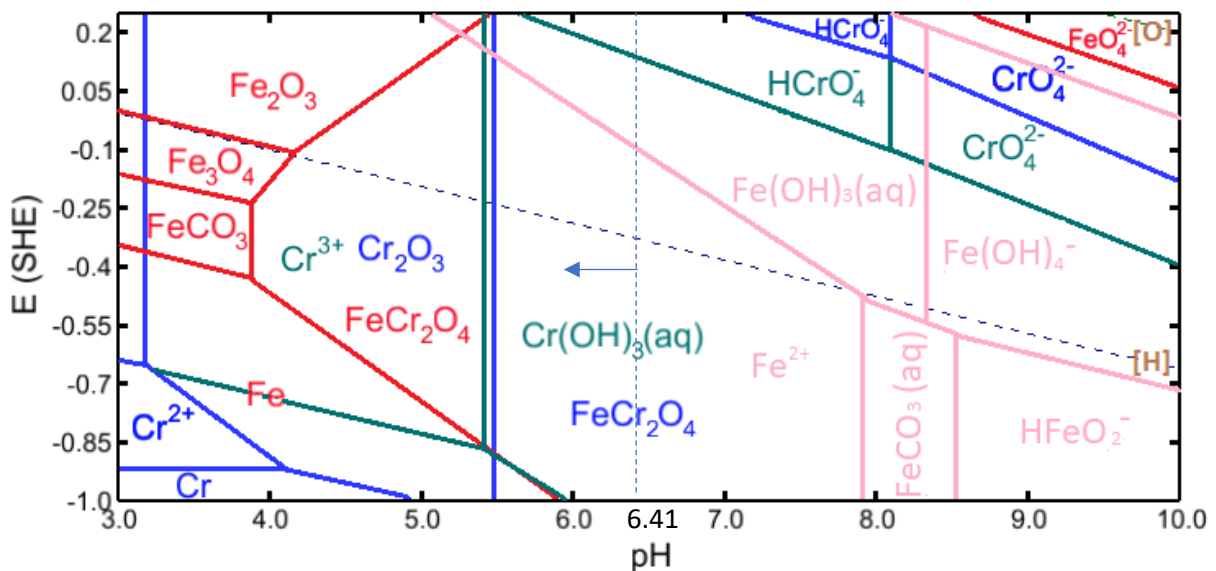
385

386   **Figure 15. Pourbaix diagrams for Fe-Cr-H₂O-CO₂-Cl⁻ systems in the CO₂-saturated solution**

387   **at 200°C and 2.7 bar p_{CO2}.**
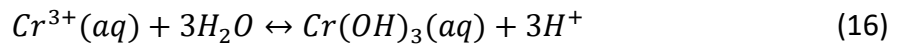
31

388   ***4.2 The compositions of double-layered corrosion scales for 3Cr at 28.5 bar of CO₂ partial***

389   ***pressure***

390   ***4.2.1 The development of the double-layered corrosion scales for Fe -H₂O-CO₂-Cl⁻ systems at***

391   ***p_{CO2} of 28.5 bar***

392   Figure 16 indicates the constructing Pourbaix diagram at 28.5 bar p_{CO2} and 200°C for Fe-H₂O-

393   CO₂-Cl⁻ systems. As increasing the p_{CO2} to 28.5 bar, FeCO₃ becomes the thermodynamically

394   favorable corrosion product, which presents as the extension of the thermodynamically

395   stable region to the lower pH and noble potential in Figure 16.

396   Despite the enlarged FeCO₃ region, no thermodynamically stable solid phase can be formed

397   in the initial stages of a system dominating by the hydrogen evolution reaction at a low pH of

398   5.39. The accumulation of Fe²⁺ and Cr³⁺ ions and consuming the acidity are via the cathodic

399   reactions. The precipitation of FeCO₃ is via the following reaction as well as the surface pH

400   increased at least to 5.91 and marked as boundary ⑤ as shown in Figure 16. Again, the

401   Pourbaix diagram only considers the thermodynamic reactions, the precipitation of FeCO₃

402   over time can be controlled by the crystal kinetics.

$$Fe^{2+}(aq) + H_2CO_3(aq) \leftrightarrow FeCO_3(s) + 2H^+(aq) \qquad (17)$$
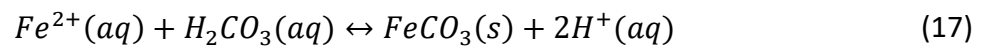
$$pH_{Fe^{2+}/FeCO_3} = -\log\left(K_{(Fe^{2+}/FeCO_3)} \cdot c_{Fe^{2+}} \cdot c_{H_2CO_3}\right)^{\frac{1}{2}} \cdots\cdots\cdots line\ ⑤ \qquad (18)$$

32
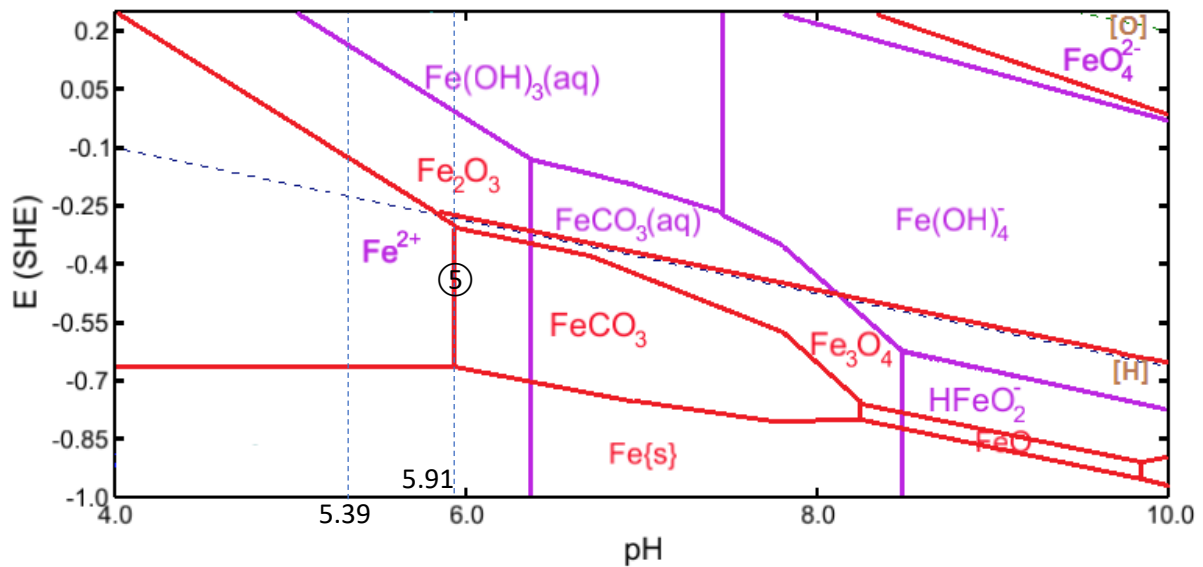
Figure 16. Pourbaix diagrams for Fe-H₂O-CO₂-Cl⁻ systems in the CO₂-saturated solution at 200°C and 28.5 bar p_{CO2}.

4.2.2 The development of the inner corrosion scales for the Fe-Cr-H₂O-CO₂-Cl⁻ systems at 200°C and p_{CO2} of 28.5 bar

The presence of Fe^{2+} and Cr^{3+} ions affects the thermodynamically stable product formed on the 3Cr steel surface. Figure 17 illustrates the constructing Porbaix diagram for the Fe-Cr-H₂O-CO₂-Cl⁻ systems based on the mass loss results after 20 hours in comparison to the Fe-H₂O-CO₂-Cl⁻ systems at 28.5 bar of p_{CO2} (Figure 16). Refer to the calculate pH of 5.39 and corrosion potential of -0.57 V/SHE in the system, the corrosion scales of $FeCr_2O_4$ and $Cr(OH)_3$ become thermodynamically stable, and this consistent with the XRD and Raman measurements for the inner layer compositions. The growth of the inner layer directly depresses the general corrosion rates, and reactions (15) and (16) cause the local acidification at the matrix/inner layer interface, resulting in the inner corrosion layer develops non-uniformly over long-term immersion time of 120 hours as shown in 7b.
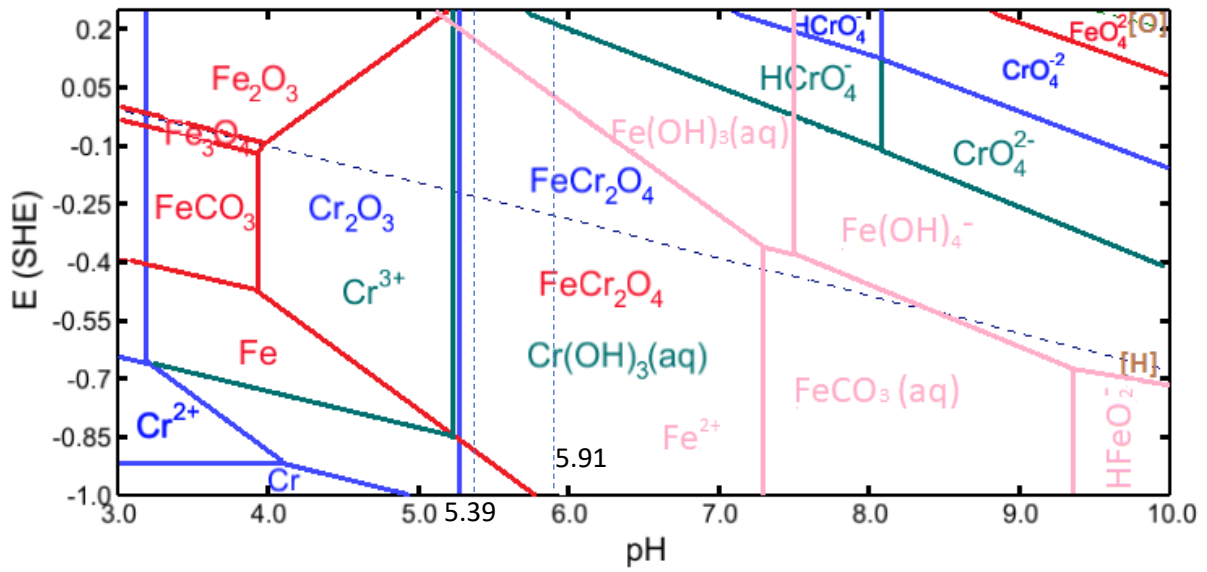
Figure 17. Pourbaix diagrams for Fe-Cr-H_2O-CO_2-Cl^- systems in the CO_2-saturated solution at 200°C and 28.5 bar p_{CO2}.

4.3 Localised corrosion of 3Cr steels induced by the formation of the inner layer containing Cl^- ions

3Cr suffered severe anodic dissolution in the initial stages at a high temperature of 200°C, which is believed to be promoted by the presence of Cl^- [25, 26]. The Cl^- ions are preferentially adsorbed on the bare surface：

$$Fe(s) + Cl^-(aq) \leftrightarrow [FeCl]^-(ads) \tag{19}$$
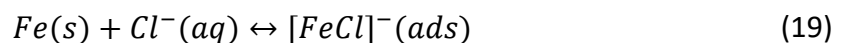
The formation of $[FeCl]^-$ is believed to act as a catalyse, promoting the anode dissolution process by the following mechanism [28, 29]:

$$[FeCl]^-(aq) + H_2O(l) \leftrightarrow [Fe(Cl)OH]^-(ads) + H^+(aq) + e^- \tag{20}$$

$$[Fe(Cl)OH]^-(ads) \leftrightarrow [Fe(Cl)OH](ads) + e^- \tag{21}$$

$$[Fe(Cl)OH](ads) + H^+(aq) \leftrightarrow Fe^{2+}(aq) + Cl^-(aq) + H_2O(l) \tag{22}$$

34
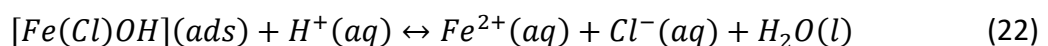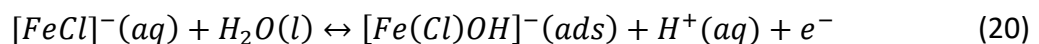
428 For 2.7 bar of p_{CO2}, the inner corrosion layer is rapidly covered the entire surface including the

429 areas beneath the outer crystalline $FeCO_3$ with low recorded corrosion rates as shown in

430 Figure 3, the Cl^- ions are blocked by the dense and compact inner layer which restrict the

431 catalytic dissolution process, the inner layer provides good corrosion protection to the steel

432 surface. The line-scans in Figure 12 c and d show no obvious Cl^- ions are distributed within the

433 inner layer. A relatively mild localised corrosion for 3Cr steel without the acceleration by Cl^-,

434 consistent with the observation of the localised corrosion shown in Figure 11.

435 However, according to the SEM images of the condition of 28.5 bar p_{CO2}, as shown in Figure

436 4, the precipitation of the Cl-rich inner layer was due to the fast anodic dissolution in the initial

437 stage, in which the positive metal irons generated and adsorbed the negative Cl^- ions, forming

438 a Cl-rich inner layer with a defective amorphous feature. The abundance of H^+ becomes to be

439 involved in the formation of the defects of the inner $Cr(OH)_3$ layer (Reaction 16), forming a

440 local positive charge region and further attracting the penetration of Cl^- ions inward. The Cl^-

441 ions accumulate at the sites where the localised acidification occurs and induce the local

442 anodic dissolution with concentrated Cl^- ions, resulting in the sediment of the unescapable Cl^-

443 ions within the inner layer and accelerates the localised attack. Hua et al.,[11] reported that

444 enrichment of Cr within the product layers formed on low Cr-containing steel exhibiting to

445 have implications for the localised corrosion. The precipitation of amorphous $Cr(OH)_3$ in the

446 inner layer at 28.5 bar p_{CO2} and 200°C is accompanied with the severe mass loss catalysed by

447 aggressive ions attack, such as Cl^-, provides a susceptibility for the penetration of Cl^-, resulting

448 in the generation of the localised corrosion as shown in Figure 10.

35

449   ***4.4 Proposed evolution mechanism of the corrosion scales on the surface***

450   Figure 18 indicates the schematic diagram of the formation and evolution of the corrosion

451   scales on the 3Cr steel surface at 200°C and different p_{CO2}. The double-layered corrosion

452   scales at low p_{CO2} of 2.7 bar mainly composes Fe_3O_4 and scattered $FeCO_3$ crystals in the early

453   period. The covered inner layer on the substrate plays a major role in the protection of the

454   surface compared to the outer crystalline $FeCO_3$ layer. The enrichment of Cr improved the

455   protectiveness of the inner layer via the formation of the $FeCr_2O_4$ and $Cr(OH)_3$ but the increase

456   in localised corrosion where the local acidification occurs during the inward growth by local

457   anodic reactions. No obvious Cl^- accumulation exists in the corrosion scales, corresponding to

458   a relatively low localised corrosion attack for the 3Cr samples immersed in the solution at 2.7

459   bar of p_{CO2} and 200°C.

460   For 28.5 bar p_{CO2}, the inner layer mainly composed a mixture of $FeCr_2O_4$ and $Cr(OH)_3$; and the

461   outer layer is a compact and dense $FeCO_3$ layer. The formation of dominate $Cr(OH)_3$ at

462   relatively low pH suggests the amorphous and highly defective features for the inner layer.

463   The Cl^- ions easily diffuse into the defects of the inner layer, accelerating the localised

464   corrosion at the interface where the local dissolution is catalysed by Cl^-. The formation of the

465   Cr-riched inner layer and outer crystalline $FeCO_3$ layer enhances the protectiveness for the

466   general corrosion. However, the results suggest that the corrosion scales are disability against

467   the localised attacks in a Cl^--containing environment at 200°C and 28.5 bar p_{CO2}.
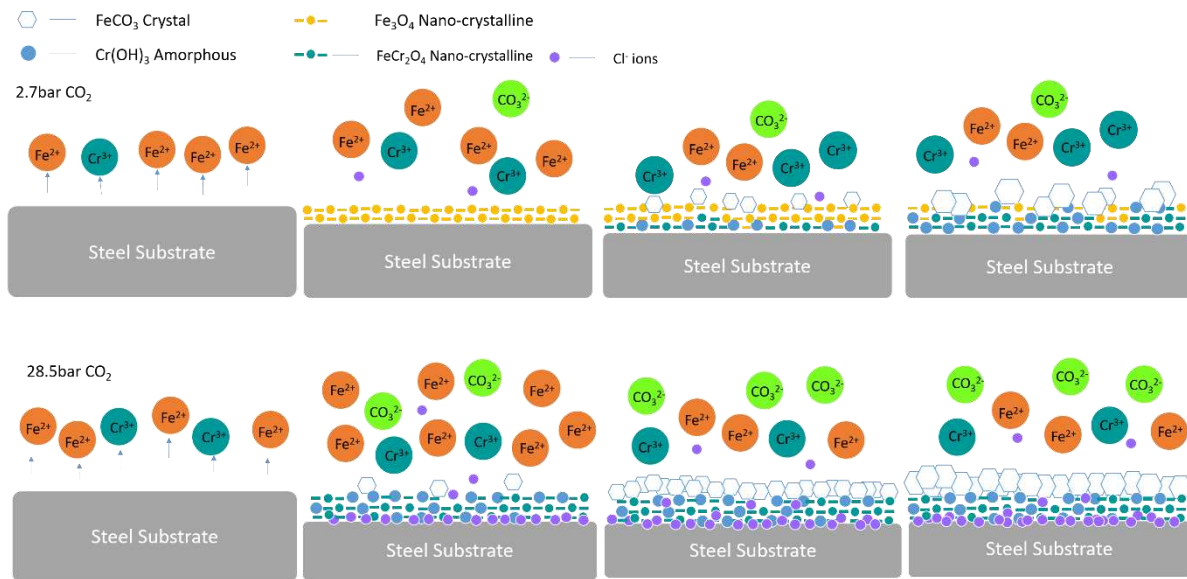
Figure 18. Schematic diagrams of the evolution of corrosion scales for 3Cr steels at 200°C and different p_{CO2}.

5.0 Conclusions

The characterisation of the double-layered corrosion scales on the surface and the localised corrosion behaviour of 3Cr steel under a geothermal environment has been investigated at 2.7 and 28.5 bar of p_{CO2} for a constant temperature of 200°C. The study is mainly focused on the corrosion behaviour and the evolution of the corrosion product scales on the 3Cr surface. The following main conclusions can be made:

1. At 200°C and 2.7 bar of p_{CO2}, the developed corrosion product scales on 3Cr include three periods: for period I, the formation of inner Fe_3O_4-dominated layer (containing small amount of $Cr(OH)_3$) and the precipitation of outer $FeCO_3$ crystals; Stage II, Fe_3O_4 transited to $FeCr_2O_4$ and $Cr(OH)_3$ precipitation. Stage III, the growth of the crystalline $FeCO_3$.

2. The outer layer of corrosion product scales for 3Cr steel at 200°C and 2.7 bar of p_{CO2} are

37

482   scattered crystalline $FeCO_3$ outer layer and an inner layer composes of $FeCr_2O_4$ and

483    $Cr(OH)_3$ over 120 hours of exposure.

484   3. For the condition of 28.5 bar of p_{CO2}, the corrosion scales are mainly comprised of the

485   outer crystalline $FeCO_3$ and inner layers of $FeCr_2O_4$ and $Cr(OH)_3$. The formation of the

486   crystalline $FeCO_3$ layer is dense and compact after 5 hours in comparison to the scattered

487    $FeCO_3$ crystals observed at 2.7 bar of p_{CO2}.

488   4. The formation of the corrosion layers at 28.5 bar of p_{CO2} acts as a barrier against general

489   corrosion. However, the localised corrosion is high due to the level of Cl^- content within

490   the inner layer at 28.5 bar of p_{CO2}, which accelerates the localised attacks compared to 2.7

491   bar after 120 hours of immersion.

492

499

500   *6.0 Reference*

501   1.   L. Xu, S. Guo, C. Gao, W. Chang, T. Chen, and M. Lu, Influence of microstructure on

502   mechanical properties and corrosion behavior of 3% Cr steel in CO_2 environment.

503   Materials and Corrosion, 2012. 63(11): p. 997-1003.

504   2.   T. Muraki, T. Hara, and H. Asahi. Effects of chromium content up to 5% and dissolved

505   oxygen on CO_2 corrosion. in CORROSION 2002. 2002. NACE International.

506   3.   M. Ueda. and H. Takabe. The formation behavior of corrosion protective films of low

507   Cr bearing steels in CO_2 environments. in CORROSION 2001. 2001. NACE International.

508   4.   B. Kermani, J.C. Gonzales, G.L. Turconi, L. Pigliacampo, T. Perez, and C. Morales.

509   Window of application and operational track record of low carbon 3Cr steel tubular.

510   in CORROSION 2006. 2006. NACE International.

511   5.   J. Zhu, L. Xu, and M. Lu, Electrochemical impedance spectroscopy study of the

512   corrosion of 3Cr pipeline steel in simulated CO_2-saturated oilfield formation waters.

513   Corrosion, 2015. 71(7): p. 854-864.

514   6.   S. Guo, L. Xu, L. Zhang, W. Chang, and M. Lu, Characterization of corrosion scale

515   formed on 3Cr steel in CO_2-saturated formation water. Corrosion Science, 2016. 110:

516   p. 123-133.

517   7.   Y. Lu, H. Jing, Y. Han, and L. Xu, Effect of temperature on the 3Cr low-alloyed steel

518   initial corrosion behavior in CO_2 solution. Materials Chemistry and Physics, 2016. 178:

519   p. 160-172.

520   8.   H.F. Liu, D. Han, J. Sun, and Y. Hua. Applicability of 3Cr-N80 Steel and N80 Steel in

521   Oilfield CO_2 Environment. in CORROSION 2019. 2019. NACE International.

522   9.   W. Li, L. Xu, L. Qiao, and J. Li, Effect of free Cr content on corrosion behavior of 3Cr

523   steels in a CO_2 environment. Applied Surface Science, 2017. 425: p. 32-45.

524   10.   B. Wang, L. Xu, G. Liu, and M. Lu, Corrosion behavior and mechanism of 3Cr steel in

525   CO_2 environment with various Ca^{2+} concentration. Corrosion Science, 2018. 136: p.

526   210-220.

527   11.   Y. Hua, S. Mohammed, R. Barker, and A. Neville, Comparisons of corrosion behaviour

528   for X65 and low Cr steels in high pressure CO_2-saturated brine. Journal of Materials

529   Science & Technology, 2020. 41: p. 21-32.

530   12.   C. Chen, M. Lu, D. Sun, Z. Zhang, and W. Chang, Effect of chromium on the pitting

531   resistance of oil tube steel in a carbon dioxide corrosion system. Corrosion, 2005. 61(6):

532   p. 594-601.

533   13.   X. Lin, W. Liu, F. Wu, C. Xu, J. Dou, and M. Lu, Effect of O_2 on corrosion of 3Cr steel in

534   high temperature and high pressure CO_2–O_2 environment. Applied Surface Science,

535   2015. 329: p. 104-115.

536   14.   L. Wei, and K. Gao, Understanding the general and localized corrosion mechanisms of

537   Cr-containing steels in supercritical CO_2-saturated aqueous environments. Journal of

538   Alloys and Compounds, 2019. 792: p. 328-340.

539   15.   ASTM, E3-01. 2002: Standard Practice for Preparation of Metallographic Specimens.

540   Annual Book of ASTM Standards, ASTM.

541   16.   ASTM, E 407–99, Standard Guide for Microetching Metals and Alloys. American

542   Society for Testing Materials.

40

543   17.   Y. Hua, S. Xu, Y. Wang, W. Taleb, J. Sun, L. Zhang, R. Barker, and A. Neville, The

544   formation of $FeCO_3$ and Fe_3O_4 on carbon steel and their protective capabilities against

545   CO_2 corrosion at elevated temperature and pressure. Corrosion Science, 2019. 157: p.

546   392-405.

547   18.   Y. Hua, R. Barker, and A. Neville, Effect of temperautre on the critical water content

548   for general and localised corrosion of X65 carbon steel in the transport of supercritical

549   CO_2. The International Journal of Greenhouse Gas Control, 2014. 31: p. 48-60.

550   19.   ASTM, Standard G1-03, Standard practice for preparing, cleaning, and evaluating

551   corrosion test specimens. ASTM International: West Conshohocken, PA, 2003.

552   20.   ASTM, Standard G46-94, Standard guide for examination and evaluation of pitting

553   corrosion. ASTM International: West Conshohocken, PA, 2003.

554   21.   X. Yue, L. Zhang, Y. Wang, S. Xu, C. Wang, M. Lu, A. Neville, and Y. Hua, Evolution and

555   characterization of the film formed on super 13Cr stainless steel in CO_2-saturated

556   formation water at high temperature. Corrosion Science, 2019: p. 108277.

557   22.   Y. Li, T. Xu, S. Wang, B. Fekete, J. Yang, J. Yang, J. Qiu, A. Xu, J. Wang, and Y. Xu,

558   Modelling and analysis of the corrosion characteristics of ferritic-martensitic steels in

559   supercritical water. Materials, 2019. 12(3): p. 409.

560   23.   L. Xu, S. Guo, W. Chang, T. Chen, L. Hu, and M. Lu, Corrosion of Cr bearing low alloy

561   pipeline steel in CO_2 environment at static and flowing conditions. Applied surface

562   science, 2013. 270: p. 395-404.

563   24.   OLI software V -2.2 (OLI engine + CPS module), OLI System Ins., Morris Plains, NJ, 2016.

564   25.   D.D. Macdonald, Passivity–the key to our metals-based civilization, Pure and Applied

565   Chemistry. 71 (1999) 951–978.

566   26.   Y. Zhao, X. Li, C. Zhang, T. Zhang, J. Xie, G. Zeng, D. Xu, F. Wang, Investigation of the

567   rotation speed on corrosion behavior of HP-13Cr stainless steel in the extremely

568   aggressive oilfield environment by using the rotating cage test, Corrosion Science. 145

569   (2018) 307–319.

570   27.   S. Nesic, N. Thevenot, J.L. Crolet, D. Drazic, Electrochemical Properties of Iron

571   Dissolution in the Presence of CO_2 - Basics Revisited, in: NACE-96003, NACE

572   International, Denver, Colorado, 1996: p. 23.

573   28.   M.A.J. Mazumder, H.A. Al-Muallem, M. Faiz, S.A. Ali, Design and synthesis of a novel

574   class of inhibitors for mild steel corrosion in acidic and carbon dioxide-saturated saline

575   media, Corrosion Science. 87 (2014) 187–198.

576   29.   T.Tanupabrungsun, D. Young, B. Brown, S. Nesic, Construction and verification of

577   Pourbaix diagrams for CO_2 corrosion of mild steel valid up to 250 °C, in: NACE-2012-

578   1418. NACE International, NACE, 2012:p.16.

579   30.   Q. Yang , L. J. Qiao, S. Chiovelli, J. L. Luo. Effects of hydrogen on pitting susceptibility of

580   type 310 stainless steel. Corrosion, 1998, 54(8): p. 628-633.

581   31.   J. B. Sun, W. Liu, W. Chang, Z. H. Zhang, Z. T. Li, T. Yu and M. X. Lu. Characterisation and

582   formation mechanism of corrosion scales on low-chromium X65 steels in CO_2

583   environment. Acta Metall Sin 45.1 (2009): 84-90.